Universidad de Guanajuato

División de Ciencias e Ingenierías

Campus León

Flux implications from Horn B-Field Measurements on NuMI and LBNF

Thesis presented by

MIGUEL ANGEL HERNANDEZ MORQUECHO

This dissertation is submitted for the degree of

Master of Physics

Advisor

Dr. Julián Félix Valdez

Co-advisor

Dr. Laura Fields

June 4, 2019

Abstract

Neutrino studies have been going on for almost a century, the way these particles are measured has evolved and most intense and powerful neutrino sources are necessary. This work deals with analysis of two neutrino beams (NuMI and LBNF) and how the neutrino flux is modified by distortions of B field, measurements and simulations in GEANT 4 were made. For NuMI, studies of non-uniform current distributions in the Current Equalizer Section (CEQ) and a magnetic field inside the decay pipe were made. For LBNF, studies of distortions on magnetic field produced by four drain holes located at the end of each magnetic horn and the impact of them on the neutrino flux were made.

Quiero dedicar este trabajo a mis padres Miguel Ángel Hernández Rico y Sara Morquecho Romero por apoyarme en todo momento y ser los pilares de mi formación.

Acknowledgements

I would like to acknowledge the MINERνA Collaboration for all the support during my 9 months stay at Fermilab, specially to my local adviser Laura Fields, who gave me support, time and helped me since the first day that I started working. She motivated me to keep improving and working in the field of physics.

I want to say thanks to Jorge Morfin who invited me to work on MINERνA and helped me to progress on my work during this journey.

I would like to acknowledge my adviser Julián Félix and the Laboratory of elementary particles of the University of Guanajuato for helping me in my work and training during the last 5 years.

Thanks to Zarko who helped me with the Geant4 simulations, to Amit Bashyal who helped me with simulations and flux problems and Ben Messerly, Marvin, Gian and José Luis who helped me to solve a lot of code problems. Thanks to Katsuya who made the measurement for CEQ, and Zhijing and Cory who worked on the drain holes design and the simulation of B field.

I would specially like to acknowledge my family, my parents Miguel and Sara, and my brother Ignacio who motivated me to continue with my studies and have always been there to give support and happiness.

I want to say thanks to my home town friends (Yuri, Rodrigo and la pandillita) and my university friends (Karla, Raúl, Javier and Jazmín) who brought me support during this amazing adventure.

Thanks to the Latin America community in Fermilab who always made me feel like in home.

I want to acknowledge to CONACyT, DAIP and the University of Guanajuato for the economical resources that made my stay possible.

Contents

Chapter 1. Introduction

Neutrinos are particles of huge interest for physicists, studies of these particles have been going on for decades, the ways to measure them have evolved since the first time, starting with the design of experiments using nuclear bombs until the development of amazing and intense neutrino beams. In this thesis, analysis on neutrino beams, NuMI beam and LBNF, are presented. The goal is to study focusing magnetic systems and the impact on neutrino flux.

In chapter 2 some of the most important discoveries over the last 100 years on neutrino physics are described.

In chapter 3 NuMI beam line at Fermilab is presented, description of each part of the most intense neutrino beam in the world.

Chapter 4 is a brief description of the MINERνA detector, an experiment on the NuMI beam line that studies the interaction of neutrinos with targets made of water, helium, carbon, lead and iron.

In chapter 5 the design of DUNE/LBNF, the most ambitious experiment on neutrino studies, the two detectors and the neutrino beam are described.

In chapter 6 the analysis and results for studies on the focusing system of NuMI beam are presented. Flux implications from modifications of magnetic field near to the Current Equalizer Section (CEQ) and the presence of a magnetic field inside the decay pipe are discussed.

In chapter 7 analysis and results for distortions on the magnetic field due to drain holes, used as part of the cooling system for horn A of LBNF, and the impact on the neutrino flux are described.

In chapter 8 the conclusions of this thesis for studies on NuMI and LBNF are described.

Chapter 2. Neutrino studies

2.1 Neutrinos, the "undetectable" particle

At the beginning of the 20th century, there was a revolution on the field of physics with the development of the atomic theory and the development of quantum physics. The scientists tried to understand processes like radioactive disintegrations, where the studies on α rays prove the energy conservation principle, but the results for β rays were different. In 1911 Lise Meitner and Otto Hann showed that the energy for β decay "was not conserved" [15].

The β decay consists on the decay of an unstable atom in a stable atom and an electron with an electron antineutrino. In those days they did not know about the existence of the neutrinos and how to measure them, they had results where the energy was not conserved.

In 1930 Pauli wrote a letter where he mentioned the possibility of existence of a new electrically neutral particle with a mass not larger than 0.01 proton mass and basically impossible to get measured. He called this new particle neutron, one year later Enrico Fermi rename that particle to neutrino (small and neutral particle) [22].

2.2 The first measurement of a neutrino

After the World War II, with the development of nuclear bombs, physicists Frederick Reines and Clyde Cowan understood that they had an intense neutrino source. They proposed to solve the problem postulated by Pauli, which was to find the existence of the free neutrino. They focused on the inverse beta decay

$$\bar{\nu}_e + p = n + e^+. \tag{2.1}$$

The first detector was designed with 1 m^3 of liquid scintillator and photomultiplier tubes (PMT) on its boundaries. Reines and Cowan way of thinking was this: the neutrinos interact with the liquid scintillator, it produced positrons, these positrons ionize causing light flashes detected by the PMT, transforming that light pulses in to electrical pulses.

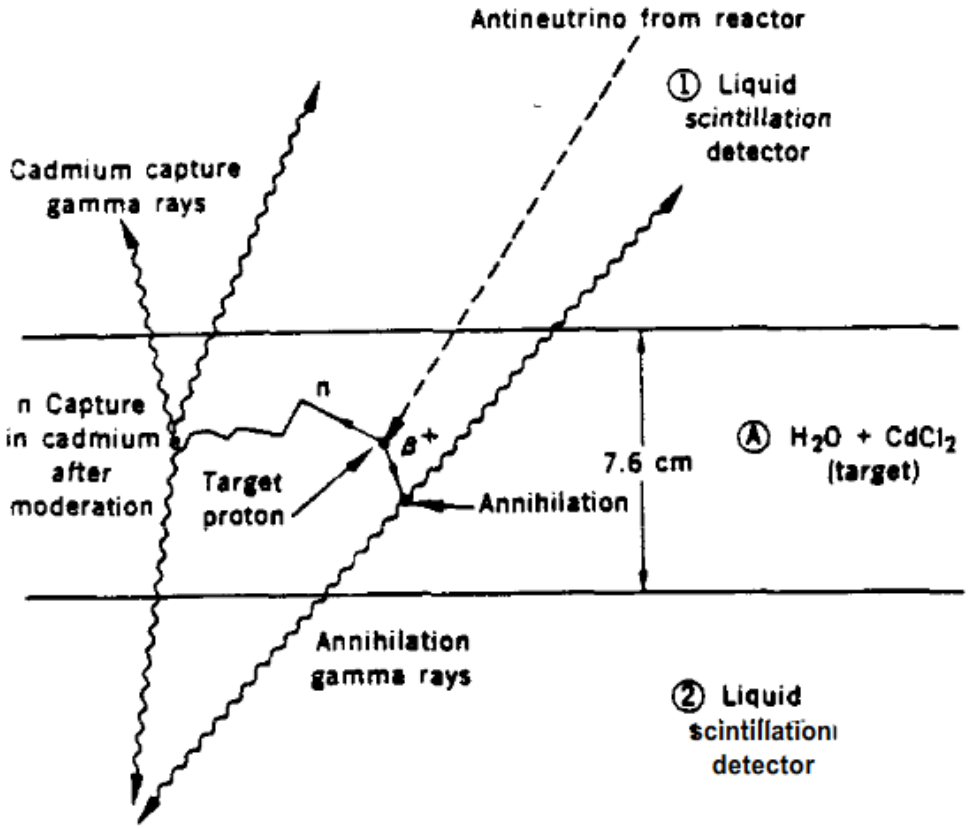

Figure 2.1. Schematic of the Cowan and Reines neutrino detector. Image taken from [24].

The idea was to use a nuclear bomb as neutrino source and keep the detector only hundred of meters away from the explosion, keeping the detector suspended in a vacuum tank with a shield for cosmic rays.

They decided to change the nuclear bomb to a fission reactor, and changed the detection technique for the schematic shown in figure 2.1. When an antineutrino from the fission reactor reaches the detector and interacts with the water with cadmium chloride, it produces a positron and a neutron. The positron interacts with an electron (annihilation) producing 2 gamma rays detected by PMT on opposite sides of the target. The neutron is captured by the cadmium producing 2 more gamma rays (those are produced about 10 microseconds later than the annihilation gammas).

The results were presented in 1956, making it the first measurement of neutrinos.

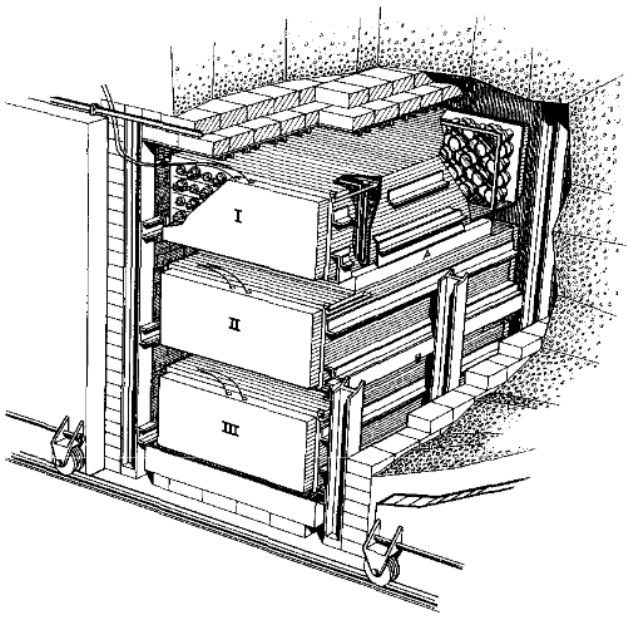

Figure 2.2. Sketch of the Cowan and Reines neutrino detector. Image taken from [24].

In 1965 the first detection of atmospheric neutrinos were made in a detector 2 miles underground in South Africa [24].

2.3 Neutrino flavours

At the beginning of 1960, the physicists only knew 3 elementary particles apart from the hadrons, the leptons (electron, muon and neutrino with the idea that there were 2 kinds of neutrinos).

In the summer of 1960 Lee and Yang pointed out that it was impossible to explain the absence of the decay

$$\mu \rightarrow e + \gamma \tag{2.2}$$

without 2 types of neutrinos. The question was $\nu_\mu \equiv \nu_e$, if that was true, the number of electrons and muons produced should be equal, if that was false, the number should be different. Lee-Yang said that muon neutrino should not produce electrons [26].

The first neutrino beam was designed, different techniques for acceleration and focus-

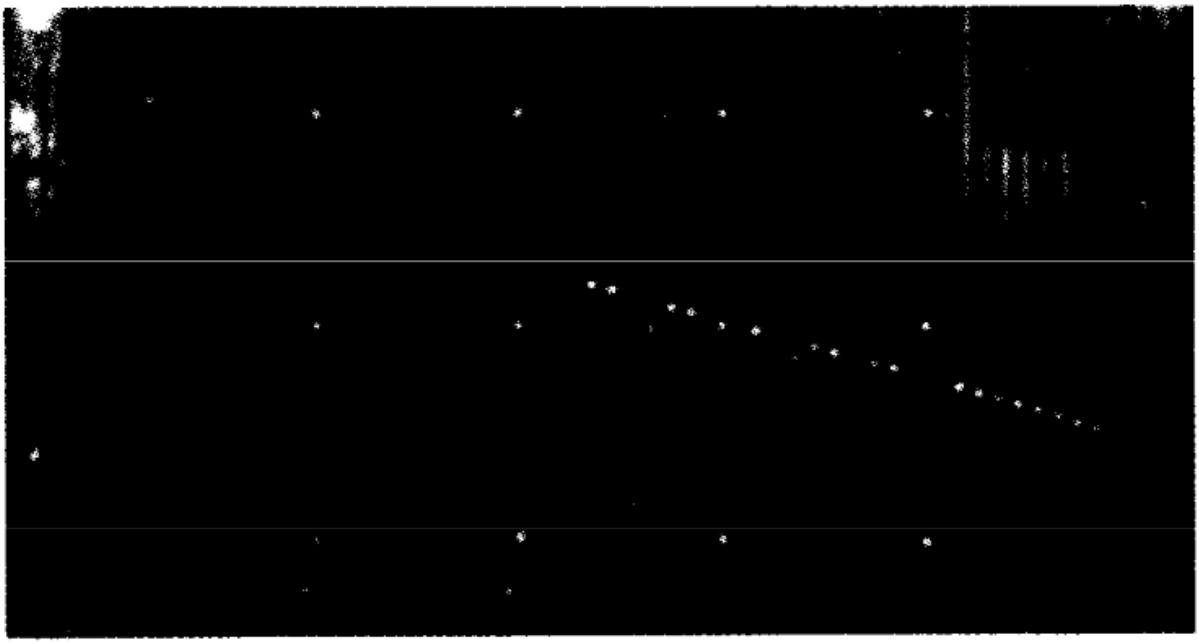

Figure 2.3. Single muon event from spark chamber. Image taken from [26].

ing systems were developed, consequently the detectors became bigger [27].

An experiment to measure the 2 types of neutrinos was developed. The Alternate Gradient Synchrotron (A.G.S.) at the Brookhaven National Laboratory was used to accelerate protons at 15 GeV. They send the protons to a beryllium target, producing a shower of pions and kaons, afterwards they put walls of steel of a dismantled cruiser. They added lead and concrete to stop the hadrons and only had neutrinos. Then there was the detector, a spark chamber (an example of an event with a muon is shown in figure 2.3).

In 1962 the observation of high energy neutrino reactions and the existence of two kinds of neutrinos were made [19].

In 1975 a third lepton was discovered, the tau "τ", hence there was evidence to think in the existence of a third neutrino too, the ν_τ. Fermilab designed an experiment to find that particle, Direct Observation of NU Tau (DONUT), in the year 2000, the first evidence of the existence of ν_τ was made [9].

Now we have 3 leptons with their respective neutrino, three neutrino flavours.

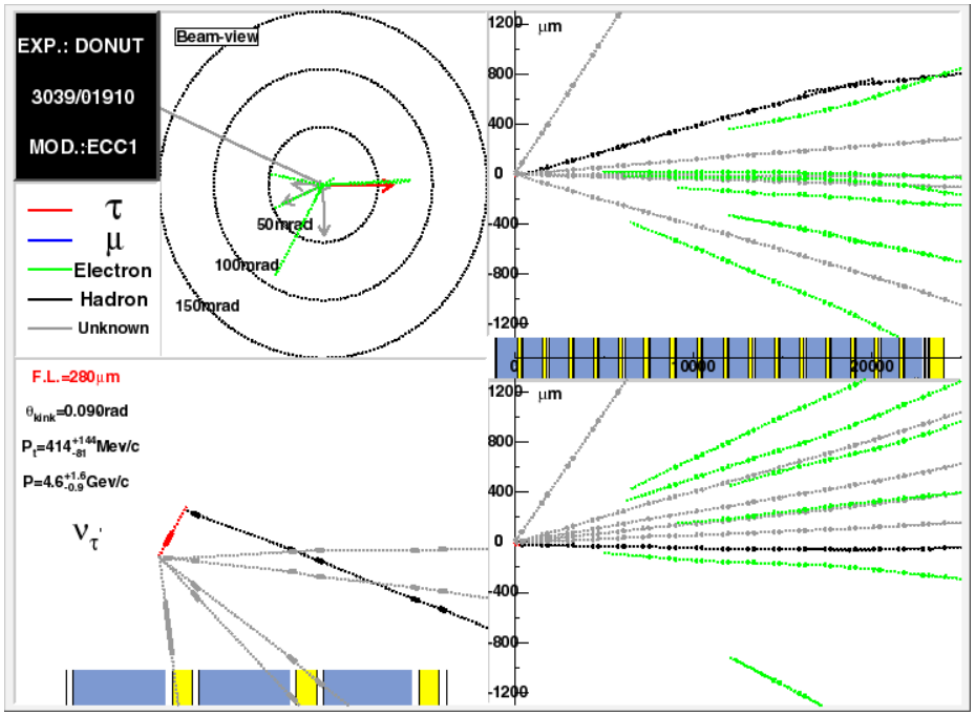

Figure 2.4. tau event (DONUT). Image taken from [9].

2.4 Neutrino oscillation and the new experiments

In 1967 Pontecorvo [23] published a paper where he explained that if neutrinos have mass, is possible for them to change flavour when they travel. It means that a neutrino of one flavour can change to another flavour, for example $\nu_e \rightleftharpoons \nu_\mu$, it is called "neutrino oscillation".

John Bahcall [33] calculated the neutrino flux produced by the Sun, and Raymond Davis [5] made the measurement of the ν_e. But the measurements were like three times smaller that the prediction, an indication that Pontecorvo was right because the Davis experiment can only measured the ν_e. The neutrino oscillation could be an explanation of the missing neutrinos.

Over the years bigger detectors were needed to detect neutrinos, the solar and atmospheric neutrino oscillation were measured in SuperKamiokande [17] and SNO [20], other experiments helps to measured properties of neutrino and neutrino oscillation.

There are experiments that do not use solar or atmospheric neutrinos to understand these particles and their interactions, for example reactor and neutrino beam. Some examples of neutrino beam oscillation experiments are MINOS (Main Injector Neutrino Oscillation Search)[12], NOνA (NuMI Off-axis ν_e Appearance)[13], and now with the development of new technologies, DUNE (Deep Underground Neutrino Experiment)[10].

The first neutrino detection was designed to use a nuclear bomb, but was made with a fission reactor. The ν_μ was detected with a neutrino beam of 15 GeV protons, the ν_τ was measured with a beam of neutrinos starting from a beam of 800 GeV protons. The next big ambitious experiment to measure neutrino properties (DUNE) will use the most intense neutrino beam on the world with protons of 60-120 GeV. To make a more exact and accurate measurement a better neutrino source is needed. The importance arises to make bigger neutrino beams and understand how it works and what has sent to the detectors.

Chapter 3. NuMI beam line

3.1 NuMI beam

The Neutrinos at the Main Injector (NuMI) beam at Fermilab, is the most powerful and intense neutrino beam in the world, is used to provide neutrinos to MINERνA, MINOS and NOνA [6].

To produce neutrinos, physicists accelerate protons at 120 GeV, they send these protons to a graphite target. The interactions between the protons and the nucleus of carbon produces hadrons, like pions and kaons. The charged particles are focused in the forward direction by 2 magnetic horns, these work like optical lenses, to a decay pipe of almost 700 m length, where the hadrons decay in neutrinos, leptons and other particles. They stop most of the particles with rocks and concrete to only have a neutrino beam. These neutrinos pass through the MINERvA and MINOS near detector (1.04 km downstream of the NuMI target) and continue to the MINOS far detector (734 km away in the Soudan Mine in Minnesota). The NuMI beam has a spill time of 10 μs with a total of 3.6×10^{13} protons on target (POT).

There are Hadron and muon monitors used to measure the neutrino flux. When the protons hits the target, hadrons are produced, most of them are pions and kaons, the predominant decays are the next ones $\pi^+ \rightarrow \mu^+ + \nu_\mu$ and $K^+ \rightarrow \mu^+ + \nu_\mu$ producing the ν_μ beam. There is one muon, or electron, for each neutrino, if we want to measure the neutrino flux produced in the NuMI beam we need to measure the number of muons produced [6].

3.2 The NuMI target and baffle

The first component of the NuMI beam is the baffle, it is used to protect the magnetic horns or other beam components. If a single pulse is not well steered it could destroy some components, to protect that, a graphite core of 1.5 m long and 57 mm in diameter (60 mm with the case) with a hole of 11 mm diameter at the center through which the proton beam passes. The baffle is fixed at the upstream of the target.

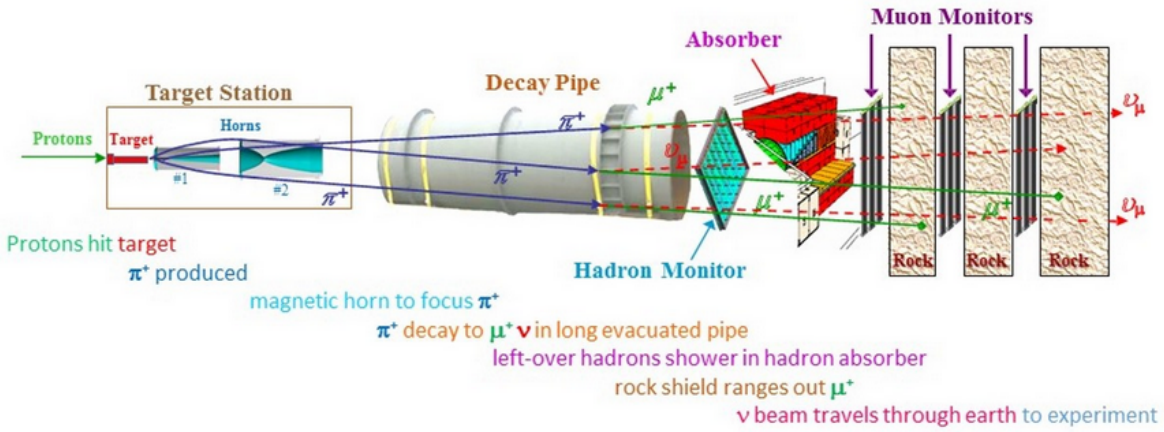

Figure 3.1. Schematic of the NuMI beam. Image taken from [14].

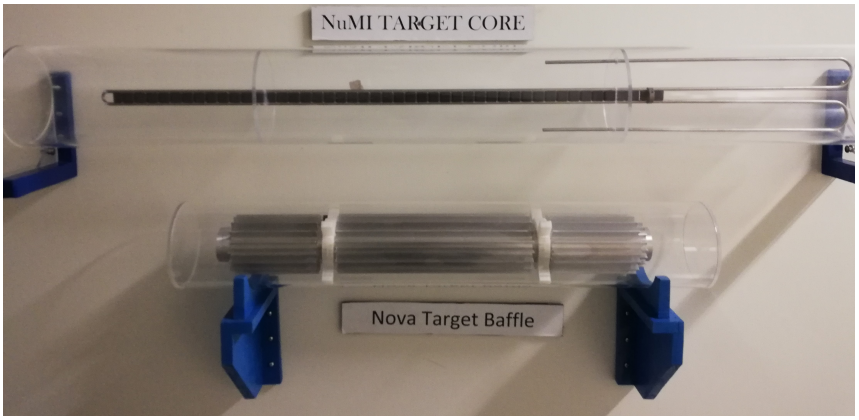

Figure 3.2. Baffle and target for NuMI beam.

The next component is the target, it is made of graphite with a density of 1.78 g/cm^3. The target has a total length of 95.38 cm and consists of a group of 47 fins, each one is 15 mm tall, 6.4 mm wide and 20 mm long. The fins are welded in two steel pipes used to transport the coolant (water). There is another horizontal fin in the target canister, 15.73 cm upstream of the main target.

To change the energy spectra of the NuMI beam (low, medium and high energy) the target and the baffle are mounted in a carrier. The carrier works remotely to avoid people entering to the radiation areas. For low energy the target is inserted 50.4 cm into the first horn.

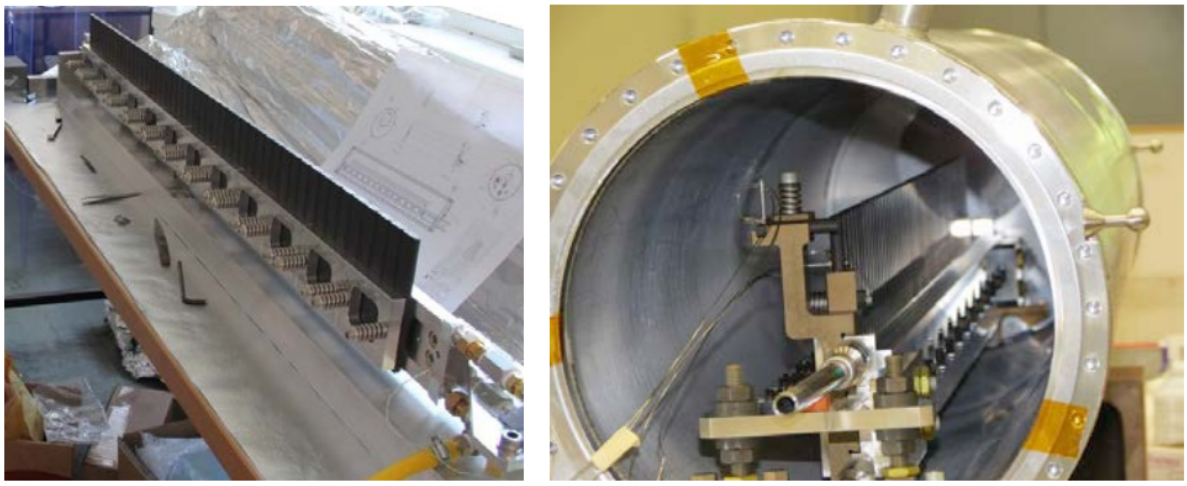

Figure 3.3. Target. Image taken from [14].

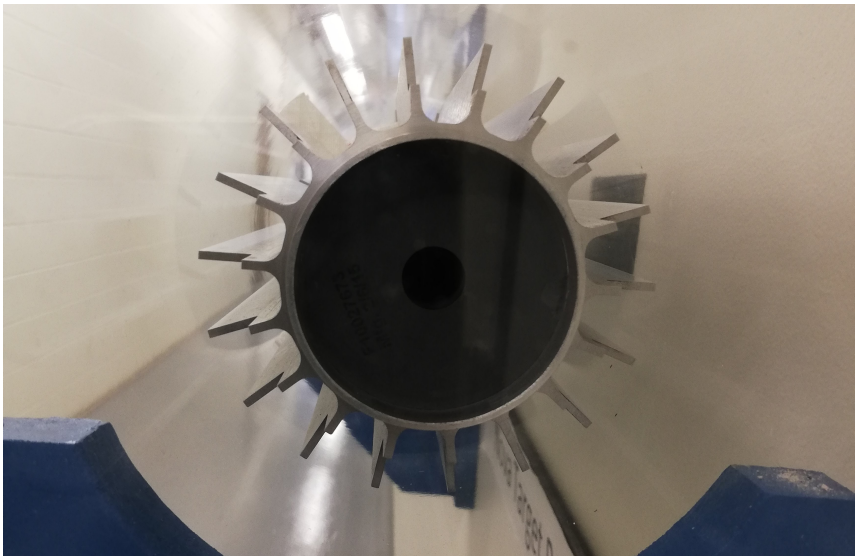

Figure 3.4. Baffle for NuMI beam.

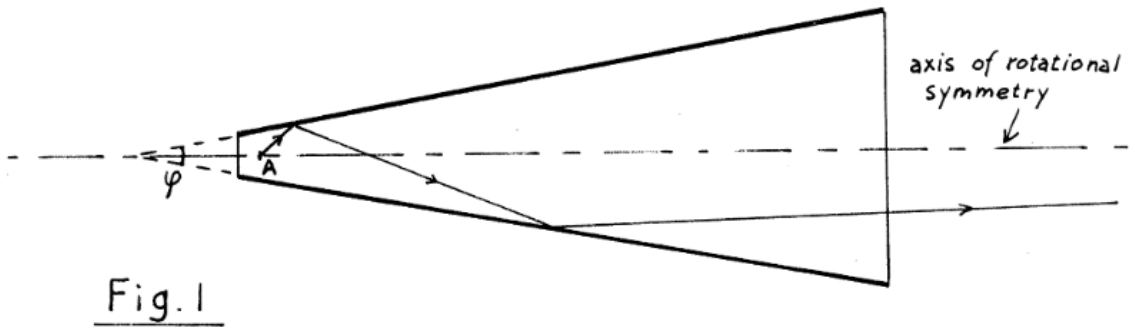

Figure 3.5. Schematic of focus device for light. Image taken from [34].

3.3 Focusing system (magnetic horns)

The first focusing device for neutrino beams was developed by Simon van der Meer in 1961[34]. He designed a magnetic lens for increasing the intensity of a neutrino beam. The idea was taken from a light focusing system, where the light is reflected in the surface of a cone several times, after each reflection the angle between the light ray and the axis decreases, fig. 3.5. Doing the same with charged particles (π and k) and a cone with two surfaces, the inner and the outer conductor, where the electrical current passes through the inner conductor and returns by the outer conductor generating a toroidal magnetic field between the surfaces, and the central cone without magnetic field, we can focus the mesons that decay into neutrinos, in consequence, we focus the neutrino beam, fig 3.6.

In 1963, Budker designed a magnetic horn with parabolic shape in the inner conductor [25], the magnetic field inside the horn does not depend on the shape of the inner conductor. With a parabolic shape, the device can focus particles of any angle of entry, with the cone shape this is not possible.

The multi-horn systems consist in multiple focusing elements, the principal advantage is that a second device could focus an improperly focused particle by the first focusing element. With a 2 horn system the divergence of the beam could be reduced by the half, with a third lens, the divergence could go down by a factor of 8 [25].

In the NuMI beam, to focus the charged hadrons produced at the target, 2 magnetic

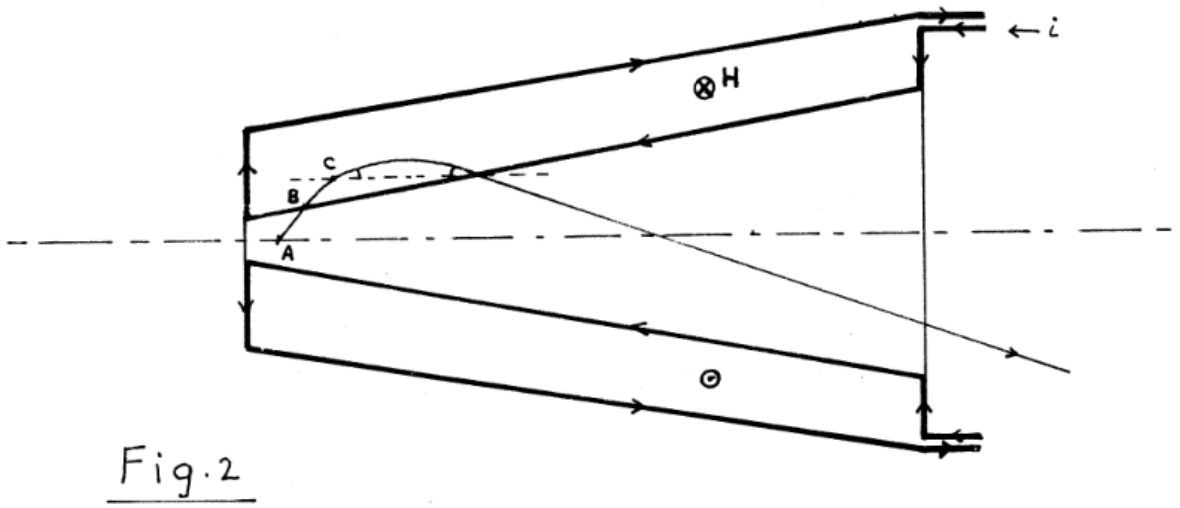

Figure 3.6. Schematic of neutrino horn. Image taken from [34].

horns are used, fig. 3.7. The distance between the front of the horn 1 and the end of the horn 2 is used for different energy configurations, 10 m, 23 m and 37 m (low, medium and high energy respectively), a schematic of the two horns is presented in fig. 3.8

The NuMI horns have an inner and outer conductor, the inner conductor has a parabolic radial profile. A pulsed electrical current (half sine wave form) with a maximum amplitude of 205 kA and duration of 2.3 ms (average flattop current equal to 200 kA) pass through the outer conductor to the inner conductor (or vice versa, depends of neutrino or antineutrino mode), producing a toroidal magnetic field inside the horn. Using the Ampere's law, this magnetic field goes like $1/R$ and is equal to zero for radii smaller than inner conductor. The field is equal to equation (3.1) where I is in kA, R in mm and B in T, the magnetic field goes from 0.1 to 3.0 T, the highest intensity is in the neck of the horn 1. The effect of the parabolic shape of the inner conductor is observed in the path length of particles trajectories inside the horns, being approximately the square of the radius at which the particle enters the conductor.

$$B = \frac{I}{5R} \tag{3.1}$$

The inner conductor of the horns are aluminum of 2 mm and 3 mm of thickness, horn1

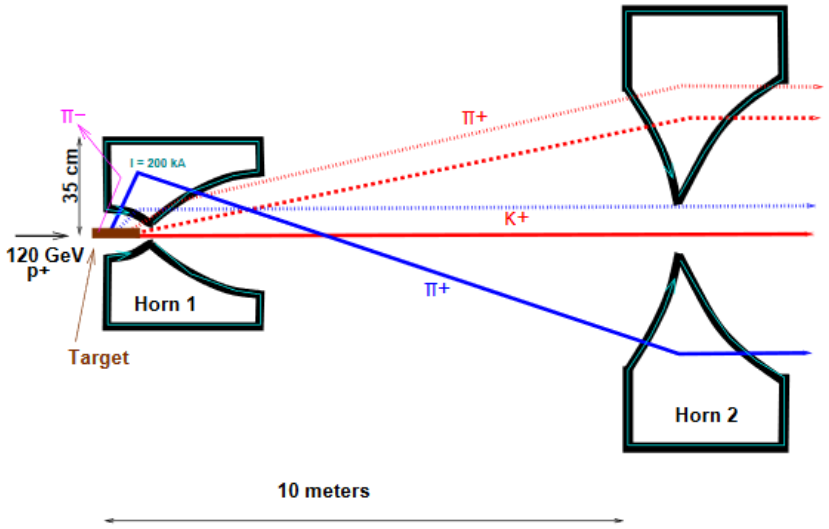

Figure 3.7. Focus system at NuMI beam. Image taken from [6]

and horn 2 respectively, with a thickness equal to 4.5 mm at the neck. The objective of using a thin horn is to avoid interactions between the horn conductor and the hadrons. A cooling system was developed to cool the inner conductors and remove heat deposited by the beam and electrical resistance by the current pulse. Each horn has a water port in 3 azimuthal position for 15 longitudinal positions and 4 drain holes at the end of the horn. At the end of the horn there is the electrical current equalizer section (CEQ), which is a straight section with length equal to the inner conductor diameter. The function of this section is to redistribute the electrical current supplied by the stripline to a uniform azimuthal sheet. The stripline is the electrical connector for input and output of the current to the horns.

3.4 Decay pipe

The decay pipe has 2 m diameter and 675 m length. The mesons propagate inside the pipe and decay in more mesons and leptons (neutrinos, muons and electrons), this process produces the neutrino beam. To have a most intense neutrino beam, the interactions between the mesons and the pipe need to be reduced; to do that, the pipe is filled with helium (low density environment). The pipe is made of steel with 0.95 cm of thickness. The pipe starts at 46 m downstream of the target. To shield the decay pipe from particles that impact the pipe walls, a concrete shielding is fixed downstream to the pipe.

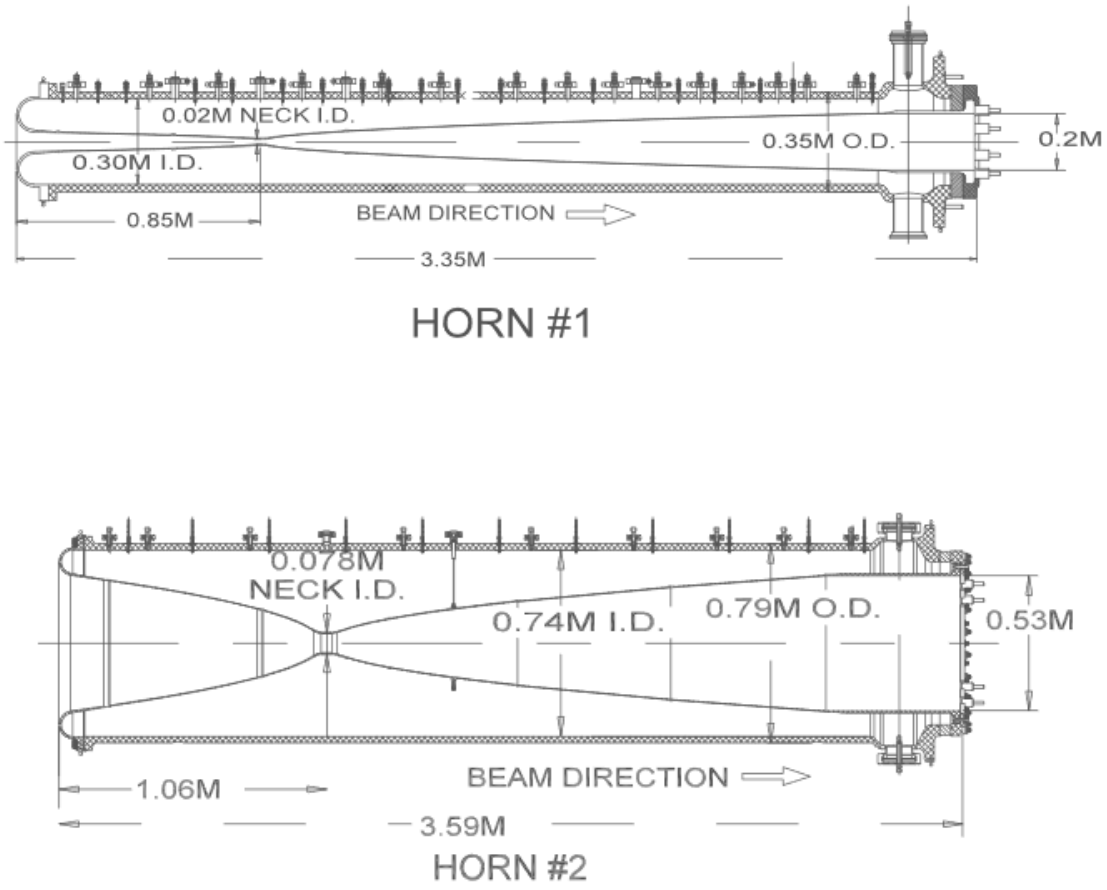

Figure 3.8. Schematic of NuMI magnetic horns. Image taken from [6].

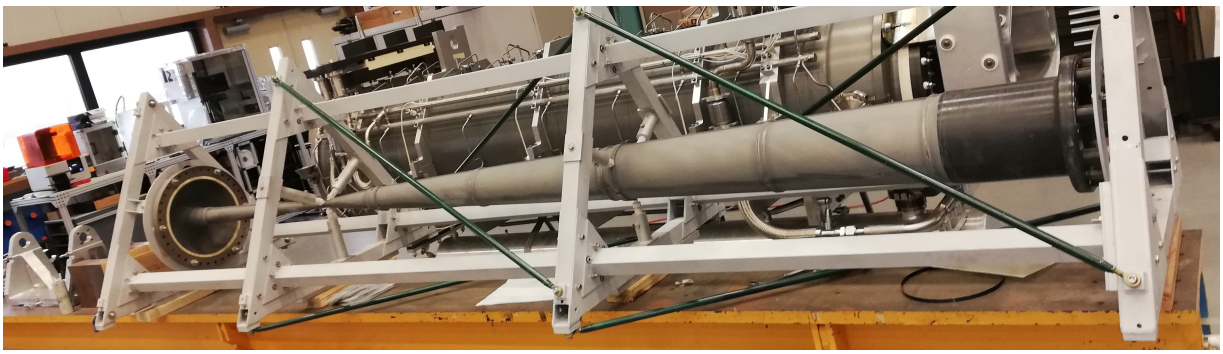

Figure 3.9. Picture of horn 1 inner conductor.

Figure 3.10. Picture of horn 2 inner conductor.

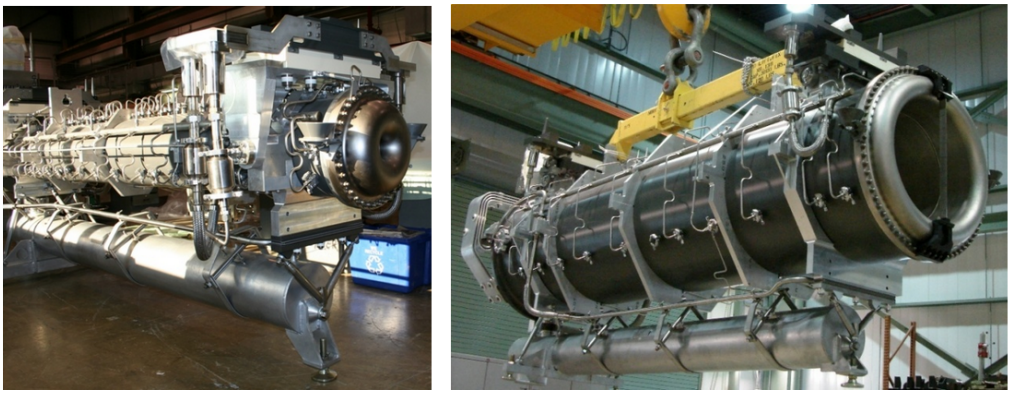

Figure 3.11. Picture of the NuMI magnetic horns. Image taken from [14].

Figure 3.12. Decay pipe. Image taken from [6].

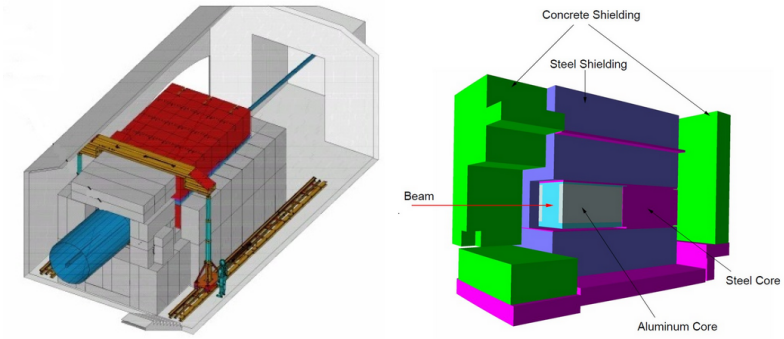

Figure 3.13. Schematic of beam absorber. Image taken from [14].

3.5 Absorber

Downstream of the decay pipe, there is a structure of aluminum, steel and concrete used to absorb the residual beam, this structure is called the absorber. It has more functions like the protection of groundwater from irradiation and limits the level of radiation in tunnel regions. The dimension of the absorber are 5.5 m wide x 5.6 m tall x 8.5 m long.

When particles pass through the decay pipe and the absorber, there are 240 m of solid dolomite rock, this is the muon shield, and next to this shield, there is the MINOS hall, where the MINERvA and MINOS detectors are running.

Chapter 4. MINERνA

4.1 MINERνA and the physics goals

The Main Injector Experiment ν - A (neutrino - nucleon) is a experiment developed to measure the interaction of neutrinos with 5 different nuclei (carbon, lead, iron, water and helium). The NuMI beam supplies the MINERνA detector with neutrinos, where the neutrinos interact with the targets and the final state particles are measured with plastic scintillator and calorimeters.

The detector was designed to complete the physics goals of MINERνA which are:

- Measurements of inclusive and exclusive signal and background reactions relevant to oscillation experiments.
- Resolve multi-particle final states, identifying the produced particles with low thresholds (energy $>$ 100 MeV and at least 10 GeV).
- Study of nuclear effects in a single beam spill.
- Study of nuclear structure functions (targets with a wide range of nucleon number A).

To solve that, the detector was designed with an active core with high spatial resolution and surrounded with electromagnetic and hadronic calorimeters. The knowledge of the electric charge is necessary, to know that, a magnetic field is required. The MINOS (Main Injector Oscillation Search) near detector is 2 meters downstream to the MINERνA detector, the MINOS detector consist of scintillator planes and magnetized iron plates that let us measure the charge and energy of particles that pass through the MINERνA detector, most of them muons μ.

The detector is made with modules, each module consists of a couple of scintillator planes made with 127 strip lines, see figure 4.2. These modules have three different orientations, X-planes, U-planes or V-planes, where the X-planes have the strips aligned

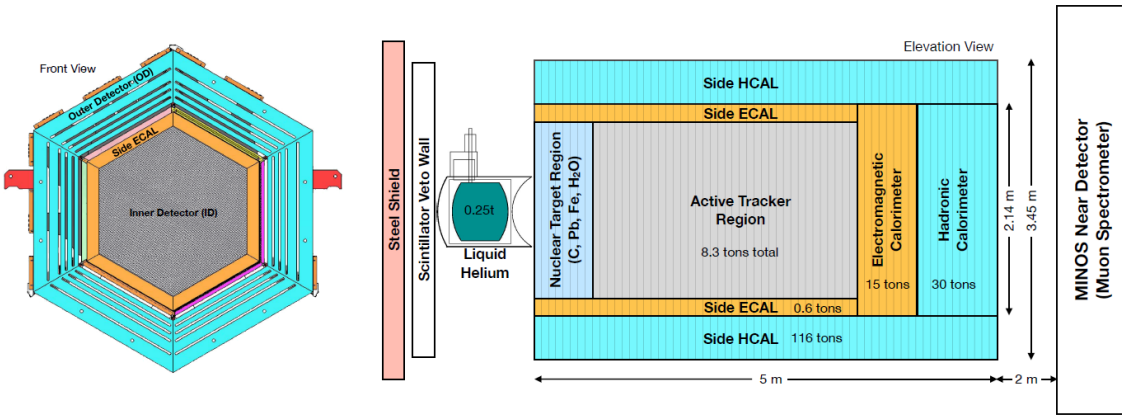

Figure 4.1. Schematic of the MINERνA detector. Image taken from [21].

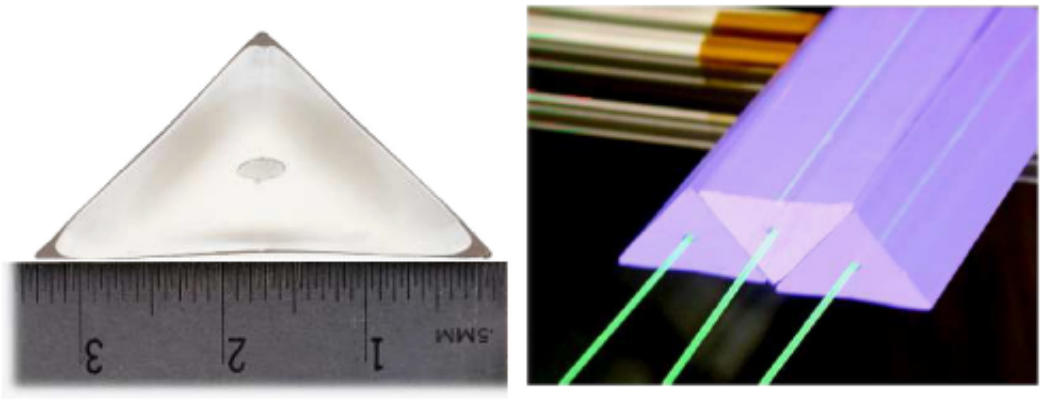

Figure 4.2. MINERνA scintillator strips detector. Image taken from [21].

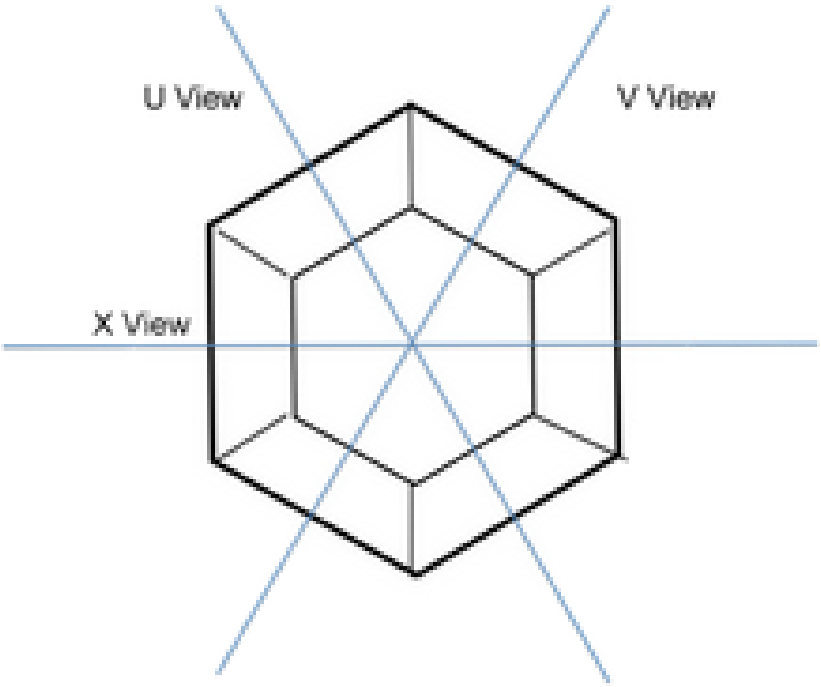

Figure 4.3. The three MINERνA views. Image taken from [3].

vertically and the U and V are rotated 60 degrees from X.

The main detector have a total of 120 modules and two sections, the inner detector (ID) and the outer detector (OD). Strip lines for ID are triangular in cross-section, for OD the strips have rectangular cross-section. The ID at the same time is divided in four different modules: the target regions is upstream, a region of nuclear targets and planes of solid scintillator, downstream is the active tracker region, a region of planes of scintillator, there are the electromagnetic calorimetry (ECAL) and the hadronic calorimetry (HCAL). The outer detector, steel frame with plastic scintillator, helps to support the structure detector. In the next sections a more detailed description of each type of module is made.

4.2 Veto wall

The first component of the detector is the veto wall, it is used to classified the muons produced between the NuMI beam and the MINERνA detector, these muons are called "rock muons". These rock muons are not produced by the interactions of a neutrino with

Figure 4.4. The MINERνA detector front view without veto wall. Image taken from [11].

the detector, basically is part of the background. The veto wall consist in 2 steel plates and 2 planes of scintillator intercalated.

4.3 Nuclear target region

Downstream to the veto wall, there is the liquid helium, a cubic meter target. Next to the liquid helium, the target region is located, see figure 4.5. There are 5 target layers made of carbon, iron and lead, downstream there is a water target, each one separated by four modules of scintillator in order to determine multiplicity of final states and energy particles. The thickness of each target is not the same, the thicker targets are upstream, the 2 thinner targets are downstream. The water target is between targets 3 and 4.

4.4 Active tracker region

The tracker region is made with 62 tracking modules, with X, U and V planes, intercalating UX and VX configurations, always with the X planes downstream. The tracker region works like an electromagnetic calorimeter, on the outer frame they have a lead collar with a thickness of 0.2 cm. When a charged particle passes through the plastic scintillator,

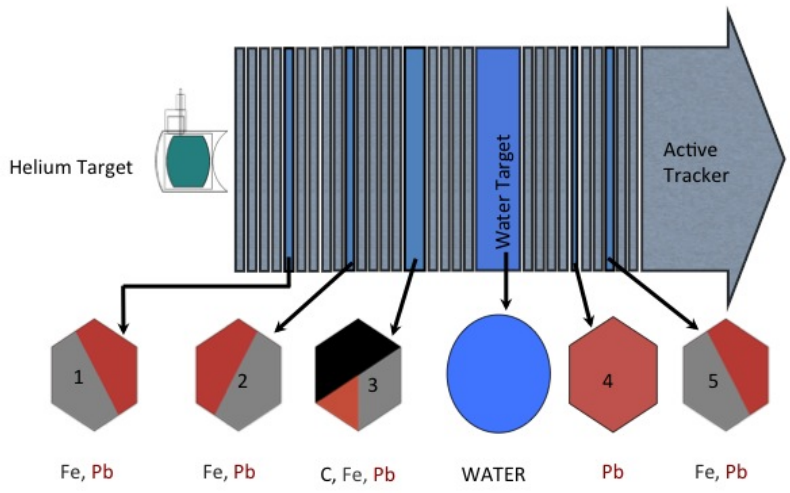

Figure 4.5. Target region along the beamline axis. Image taken from [11].

it can ionize the atoms, in consequence, free electrons are generated. These electrons recombine with atoms; photons are produced with the reaction, and travel through the optic fiber to a PMT that transforms the light into electric pulses used to measure the energy deposited by the particle.

4.5 Electromagnetic and hadronic calorimeter

The ID electromagnetic calorimeter consists of lead sheets that are 2 mm thickness, with planes of plastic scintillator between each lead sheet, with a total of 10 modules. It is used to measure the energy of photons and electrons, it has a total thickness of 4 cm of lead. The OD electromagnetic calorimeter is similar to the ID electromagnetic calorimeter, with lead of 2 mm thickness and planes of scintillator interleaved.

The ID hadronic calorimeter is made with 20 iron sheets with 2.54 cm thickness, between each iron sheet, a scintillator plane is set, it has a total thickness of 50 cm of iron. With the calorimeters, muons of 600 MeV and photons of 800 MeV are stopped. The OD hadronic calorimeter has a total thickness of 55.9 cm, with five scintillator planes of 2.5

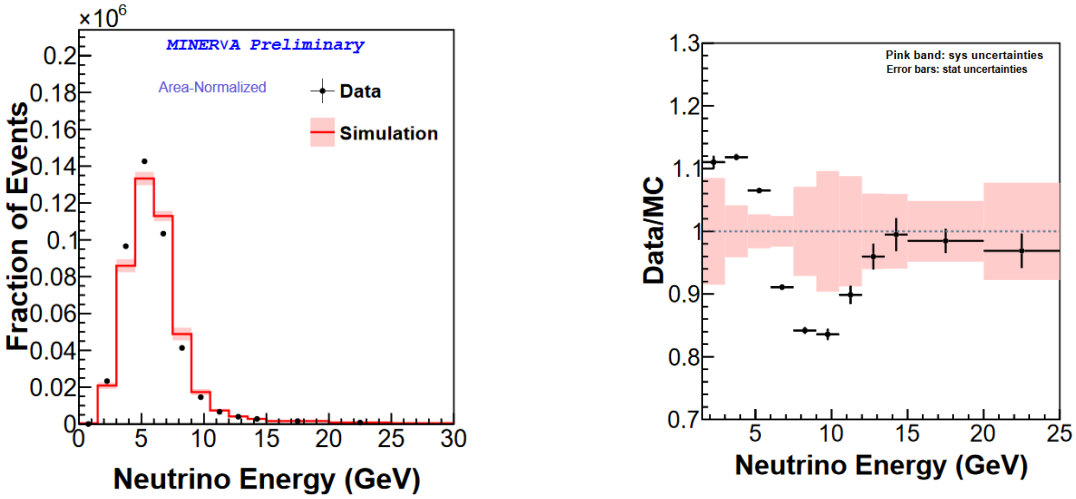

Figure 4.6. Left: Neutrino flux at MINERνA with data and MC. Right: Ratio neutrino flux at MINERνA with data over MC. Images taken from [32].

cm thickness each one, and total iron of 43.4 cm. Length enough to stop protons of 750 MeV [31].

4.6 Wiggle

When MINERνA and the NuMI beam started to run at medium energy, peak around 7 GeV, the simulation of the neutrino flux at MINERνA and the data have discrepancy up to 20% in the focusing peak region, see figures 4.6.

The first ideas about this wiggle were mis-modellings on the focusing parameters on the Monte Carlo simulation. The first studies to solve that were to add uncertainties to the beam position, horn current and offset, and target position and offset. It was obvious that we needed to learn more about the NuMI beam.

To solve the problem, a χ^2 minimization was run over 14 parameters, and a weight function was created to remove the data/MC discrepancy with the MC nominal simulation. This weight function fits for energies between 1.5 GeV and 15 GeV [32]. However, the problem is not solved yet and more studies on the simulation are necessary.

Chapter 5. LBNF/DUNE

The next generation of neutrino experiments (neutrino oscillation, neutrino astrophysics and nucleon decay) is going to be developed by Deep Underground Neutrino Experiment (DUNE), an international collaboration that includes more than 1000 scientists, over 30 countries; the laboratory of elementary particles of the University of Guanajuato [8] is part of the DUNE collaboration.

The goals for DUNE are to answer fundamental questions of universe like: the origin of the matter-antimatter asymmetry in the universe, fundamental underlying symmetries of the universe, grand unified theory of the universe, proton decay, and properties of supernovae [28].

5.1 LBNF

The Long Baseline Neutrino Facility (LBNF) is going to be the most powerful neutrino beam in the world, it is expected to be constructed by 2026 and to work for 20 years sending neutrinos from Fermilab to Sanford Underground Research Facility (SURF) in South Dakota (1300 km).

The design consists in a horn-focused neutrino beamline (three magnetic horns system based in NuMI beamline) with protons between 60 and 120 GeV from the Fermilab Main

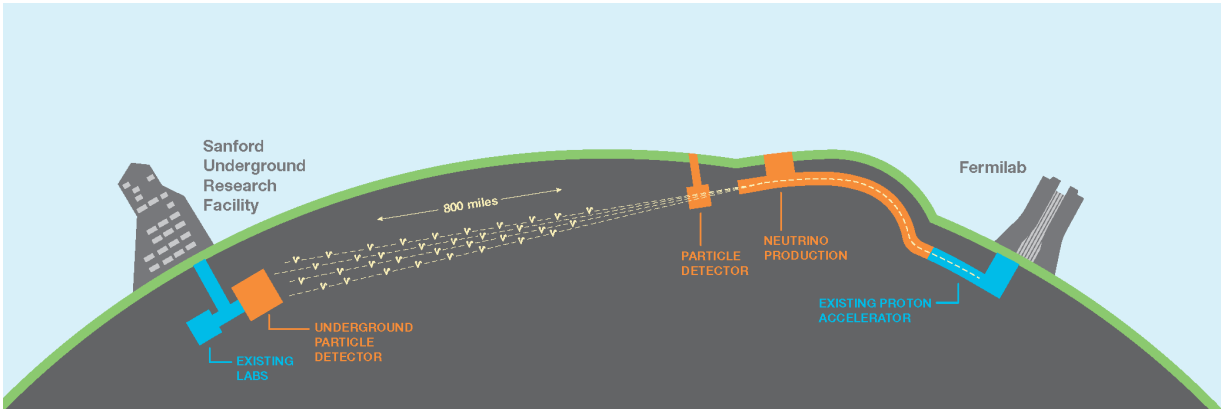

Figure 5.1. DUNE experiment. Image taken from [10].

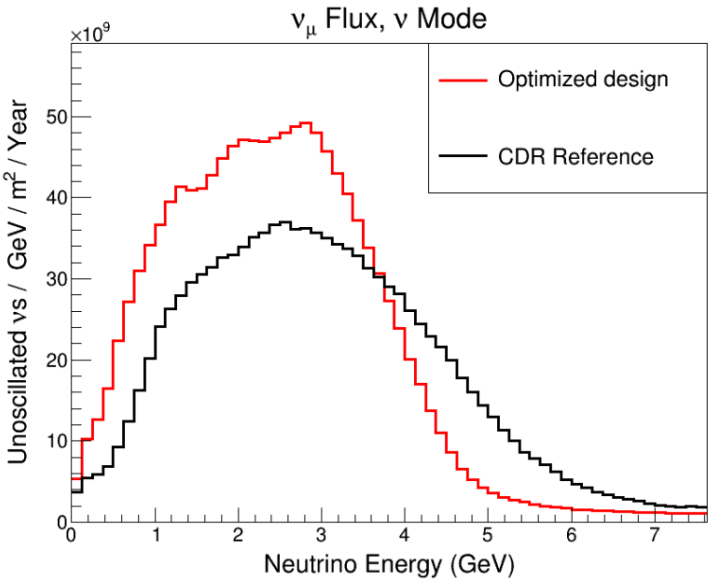

Figure 5.2. ν_μ flux in neutrino mode comparison between the Optimized design (3 magnetic horns) and the Conceptual Design Reference (CDR) presented in 2015 based in 2 magnetic horns, NuMI beam. Image taken from [30].

Injector (MI), the same used for NuMI beamline, to the target hall with a proton beam power of 1.2 MW, upgradeable to 2.4 MW [30].

At 1.2 MW the beam is expected to run with 7.5 $\times 10^{13}$ protons per cycle, with a spill duration of 1.0 $\times 10^{-5}$ s and a cycle time between 0.7 to 1.2 s.

The components of the neutrino beam are most like NuMI, the first component is the baffle (used to protect in case of mis-steering of primary beam), then there is the target, which is embed in the first horn (horn A), the second horn (horn B) is downstream to horn A, and the third horn (horn C) is 15 m downstream to horn B. The focusing system is based in three magnetic horns, the neutrino spectrum depend on the length shape, the current and the position of the horns. A decay pipe of 194 m long and 4 m of diameter filled with He is the next component, and finally the hadron absorber used to stop the remaining hadrons and only let neutrinos pass (see figure 5.3).

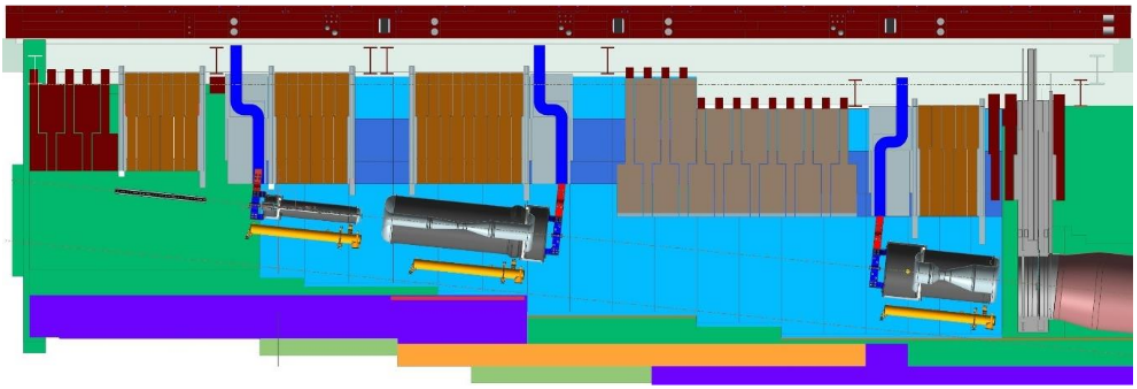

Figure 5.3. Schematic of LBNF neutrino beam, from left to right baffle, 3 focusing horns and the decay pipe. Image taken from [30].

5.2 LBNF target and baffle

The target is based on the T2K target design, modified for high energy and with twice the length. It is a 2 m cylindrical core with 16 mm of diameter, made of graphite. To improve the life time of the target, a cooling system is implemented, using high velocity helium gas, a titanium tube is needed to separate the coolant flow, and are inserted into the horn A to focus low energy pions. Upstream to the target, there is the bafflet, a little baffle used for protection, see figure 5.4. The characteristics of the target are being studied and could change until the final design.

The baffle is made to protect the inner conductor of the horns from any mis-steered beam pulse. It is the first element of the beamline and the shape depends of the configuration of horns, beam and target. The baffle consists of graphite tubular segments of 80 mm OD and 26.7 mm ID with a total length of 2 m, and it is mounted in an aluminium case, see figure 5.5.

5.3 LBNF focusing system

The focusing system for 1.2 MW was designed with 3 magnetic horns that works as optical lenses to focus mesons that decay into neutrinos. The target is inside horn A, see figure 5.6, where the MCZERO is the coordinate system origin for Monte Carlo simulations, it has a cylindrical shape for IC and an effective length of 2.218 m. 2.956 m downstream to

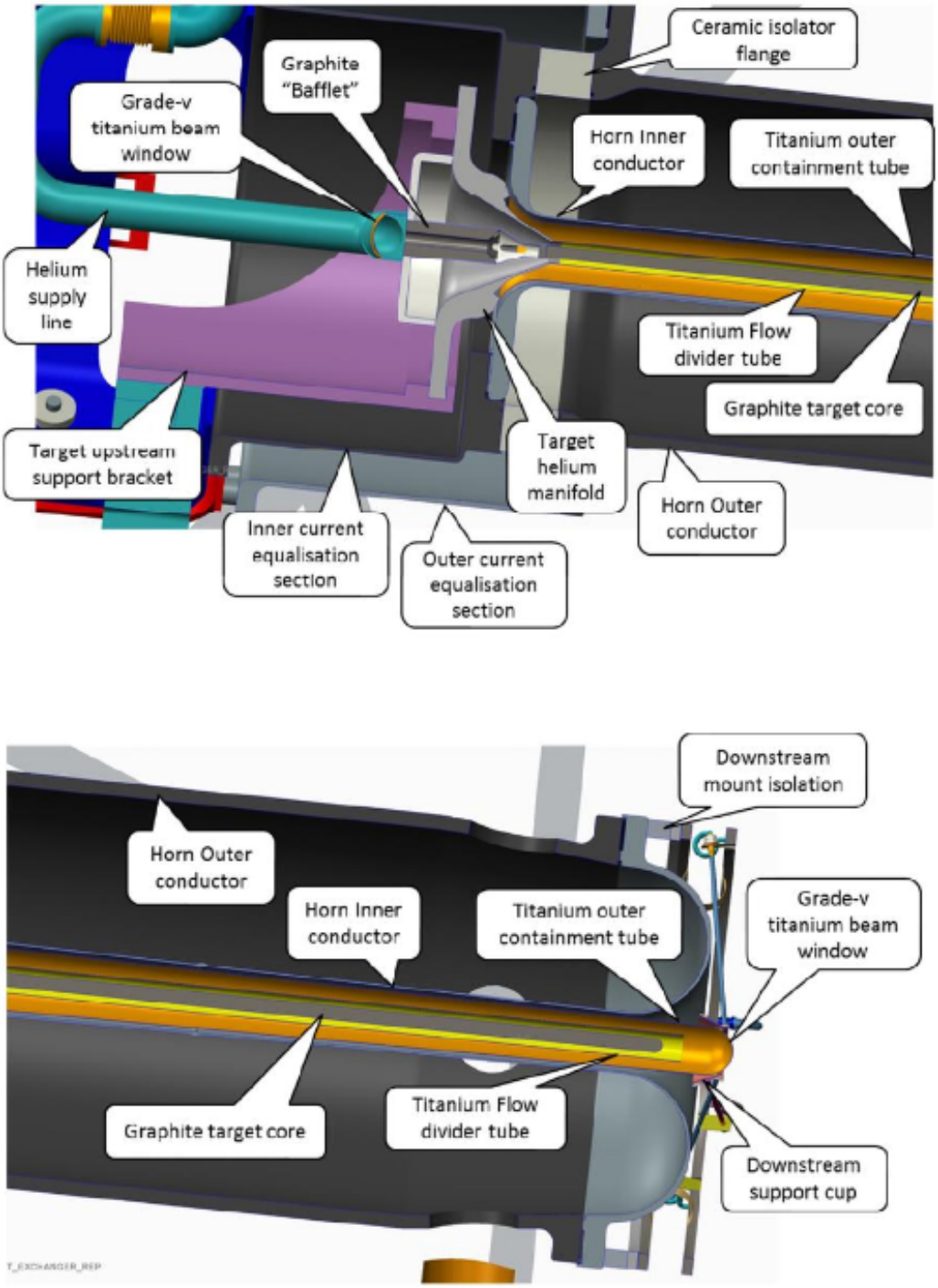

Figure 5.4. Upstream and downstream of target concept design. Image taken from [30].

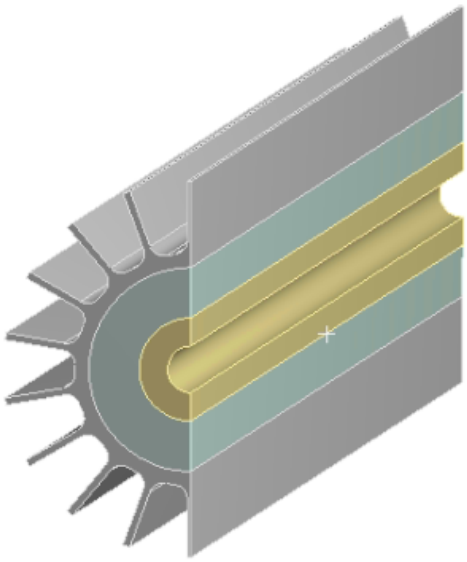

Figure 5.5. Baffle geometry for LBNF. Image taken from [30].

MCZERO is the horn B, with an effective length of 3.932 m, and with canonical shape for IC, see figure 5.7. 17.806 m downstream to MCZERO is the horn C, with an effective length of 2.184 m and conical shape for IC, see figure 5.8.

One of the most important differences between the NuMI horns and the LBNF horns, is the shape for IC, parabolic for NuMI and cylindrical and conical for LBNF. The horns were designed to be made of aluminium, with thickness of 2 mm, 3 mm and 4 mm for horns A, B and C respectively in IC. The OC thickness is 16 mm for the three horns, with the Outer OC radius equal to 220.5 mm, 650 mm and 650 mm for horns A, B and C respectively. The electrical resistance in ohms are 2.15×10^{-04} for horn A, 7.80×10^{-05} for horn B and 2.70×10^{-05} for horn C.

The stripline was designed of aluminium and is used as electrical current connector. The electrical pulses are half-sine waves with peaks of 300 kA, the pulse width is equal to 0.8 ms with repetition rate of 1.20 s, 0.9 s and 0.7 s for energy beam of 120 GeV, 80 GeV and 60 GeV respectively. The electrical resistance for the stripline, 45 meters, is equal to 3.80×10^{-04} Ω. The design for current equalizer section (CEQ) and drain holes is in progress.

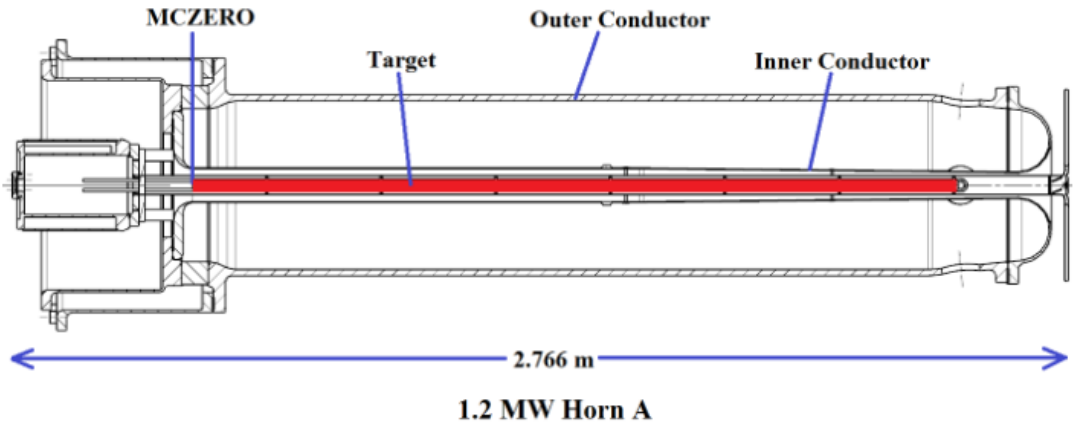

Figure 5.6. Technical drawing for horn A. Image taken from [30].

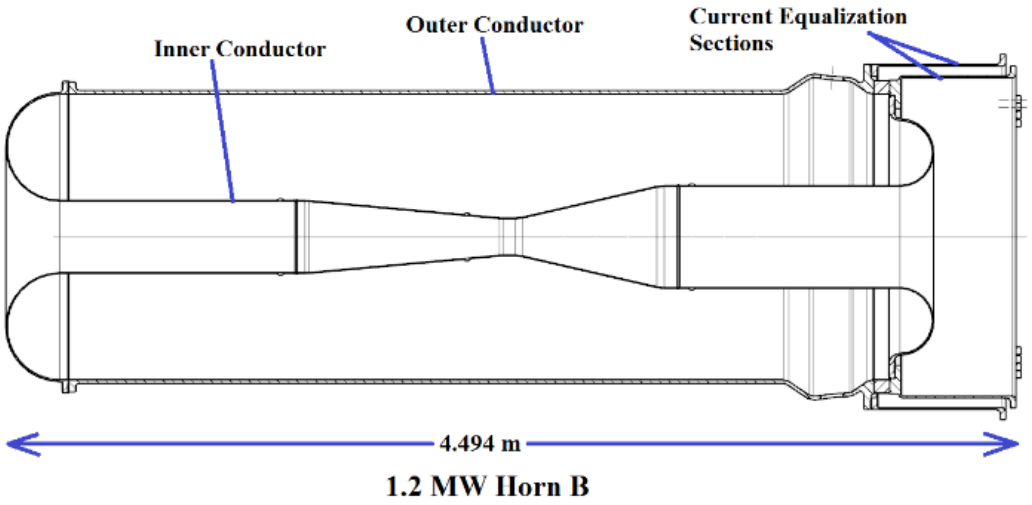

Figure 5.7. Technical drawing for horn B. Image taken from [30].

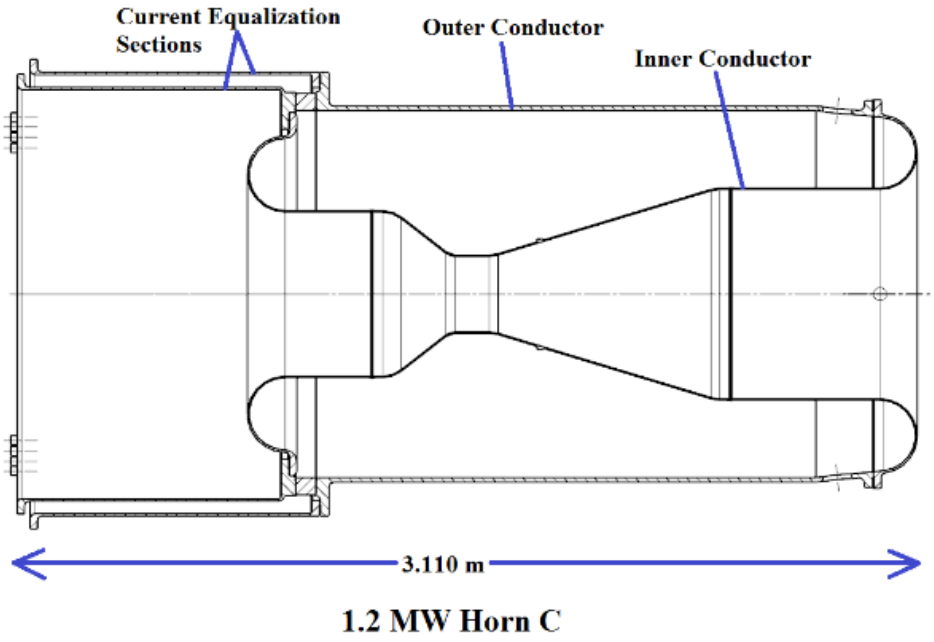

Figure 5.8. Technical drawing for horn C. Image taken from [30].

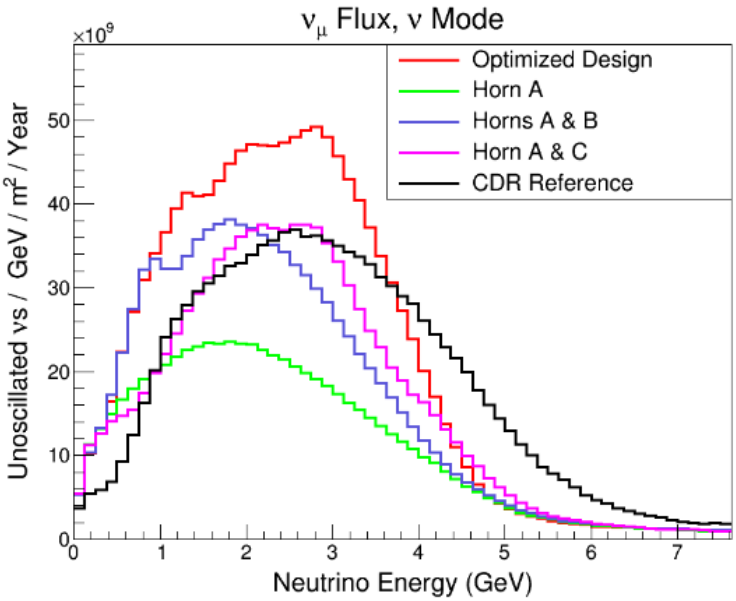

Figure 5.9. ν_μ flux at DUNE far detector with different horn configurations. Image taken from [30].

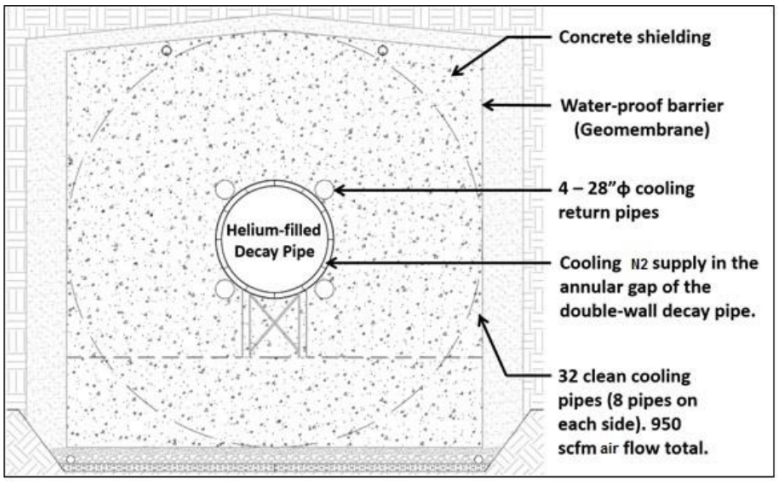

Figure 5.10. Schematic of decay pipe design for LBNF. Image taken from [30].

5.4 LBNF decay pipe

27.3 m downstream to the MCZERO there is the decay pipe, a steel pipe of 193.7 m length and 4 m of inner diameter, filled with helium, where the pions and kaons decay into neutrinos. The thickness of the decay pipe is 12.5 mm. To remove the heat in the decay pipe a second pipe located concentrically with 4.43 m inside diameter is used to circulate a cooling gas.

Tritium is created during operations in the shielding concrete. The tritiated water molecules could concentrate in drain water collected when they want to keep dry the beamline, to avoid that, two strategies were proposed, the first one is to use nitrogen instead of air to dry the decay pipe, the second one is to put a barrier system between the concrete shielding and the soil to reduce the mobility of the tritium [30]. A schematic of the decay pipe that covers all the necessities for LBNF is presented in the figure 5.10.

5.5 LBNF absorber

Downstream of the decay pipe, there is the hadron absorber, designed to absorb the hadrons that do not decay in the decay pipe. The hadron absorber is made with aluminium, steel and concrete. It consists of a core and an outer shielding [30].

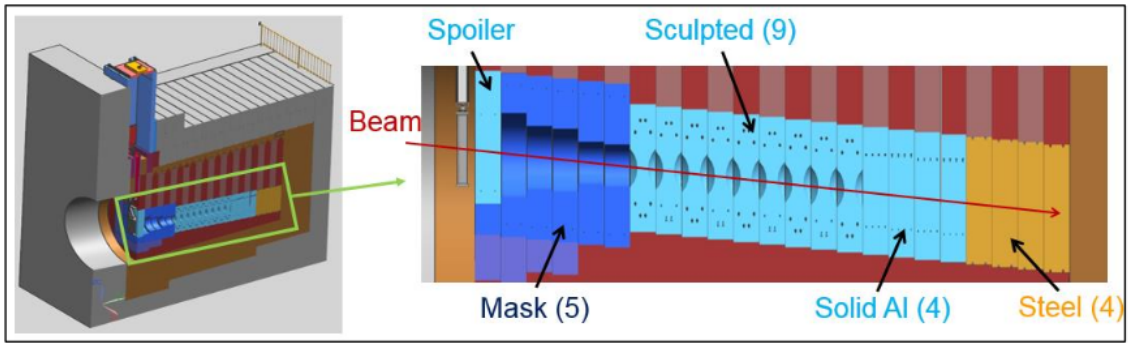

Figure 5.11. Schematic of hadron absorber design for LBNF. Image taken from [30].

The core, see figure 5.11, consists of an aluminium spoiler block, 5 aluminium mask blocks, 9 sculpted aluminium blocks and 4 solid frames of aluminium and steel. The core is cooled with water and is replaceable. The outer shielding is just a steel and concrete shielding, but the cooling system works with air. The design was made for the beam power at 2.4 MW.

5.6 DUNE detectors

To complete the goals for DUNE, the design consists in two detectors, the near, at Fermilab, and the far detector, at SURF.

The goal for DUNE Near Detector (DUNEND) is to measure the neutrino beam, energy and composition, the design is based in the NOMAD-inspired fine-grained tracker (FGT) [7], see figure 5.13, the detector is going to be at 500 m downstream to the target. The parts of the FGT are central straw-tube tracker (STT), electromagnetic calorimeter (ECAL), dipole magnet of 0.4 T and muon identifiers (MuID). The detector was designed to measure muon energy with an uncertainty better than 0.2% and hadron energy better than 0.5%, with the capacity to measure electrical charge of muons, electrons and hadrons and also high resolution for momentum measurement [29].

There are 2 designs for DUNE Far Detector (DUNEFD), each one with 4 modules of 10 kt, 12 m high, 14.5 m wide and 58 m long, a total mass of 40 kt, with Liquid Argon Time Projector Chamber (LArTPC) as detection method. The LArTPC is used to measure tracks and energy, with high efficiency in the event reconstruction. The LArTPC original

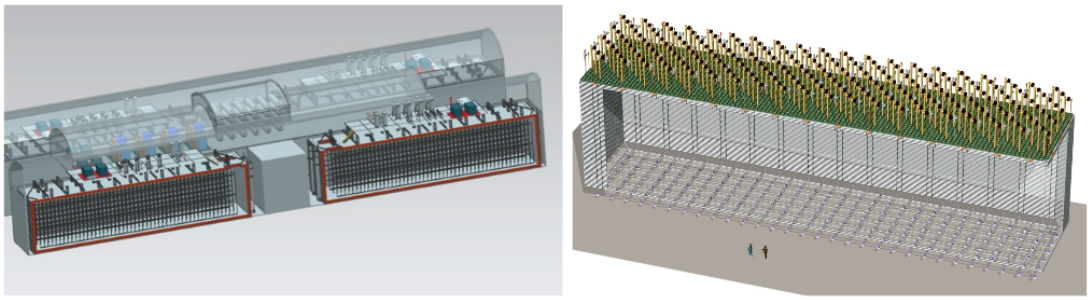

Figure 5.12. 3D models of two detectors designed for DUNE far detector. Image taken from [28].

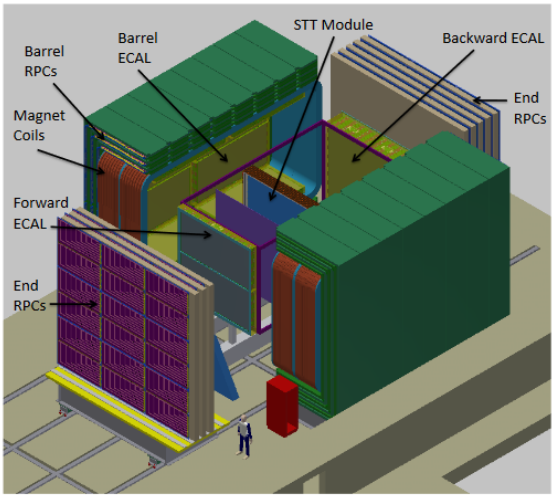

Figure 5.13. Schematic of NOMAD fine-grained tracker. Image taken from [28].

conception was designed by Carlo Rubbia in 1977, and was based in the TPC of Nygren [4]. Consist in a chamber filled with liquid Argon with electric field and a system to collect electrons. When a particle interacts with the liquid Argon, an ion pair is produced, the electrons are accelerated with a high electric field to strips that are used to collect these electrons and measure the electrical charge, with the charge and the velocity of these electrons is possible to measure the energy deposited by the particle. The idea is to use a light detection system to complement the LArTPC detection in the DUNEFD, and there are 2 different designs, see figure 5.12. The objective is to start the installation of one 10 kt module by 2021 [28].

Chapter 6. NuMI studies

As it was stated in the Wiggle Section (4.6) there is a mismatch between data and Monte Carlo. The goal in this thesis is to modify the simulation with mismodeling parameter to see how it affects the neutrino flux. Studies were made about the Current Equalizer Section (CEQ) and the Decay Pipe (DP) on the NuMI beam simulation (GEANT4) v6r3.

6.1 Shape and B field of magnetic horns

The first task made was to obtain the shape and positions of the 2 magnetic horns in the simulation. To do that, "Geantinos" were sent on the NuMI beam simulation, the "Geantinos" are virtual particles that do not interact with the detector, they are used to identify shapes and volumes.

With Geantinos it is possible to record the position when it comes in and out from a volume, with this information the inner and outer conductor for the 2 horns were obtained, see figures A.1, and A.2.

Then, "Muon Geantinos" were used to obtain the magnetic field inside the conductors, the muon geantinos are charged geantinos used to obtain the electromagnetic field of a volume. The magnetic field goes from 3.0 T (neck of horn 1) to 0.1 T (outer conductor of horn 2), see figures 6.1 and 6.2.

For horn 2 it is possible to see muon Geantinos trajectories inside the inner conductor in the magnetic field reconstruction, when the magnetic field should be equal to zero. But this is because the reference of the simulation was put in horn 1. When the nominal simulation runs, the magnetic field inside the inner conductor of each horn is equal to zero. Most of the studies were made only for horn 1. In the next section a study of the CEQ for horn 1 is described.

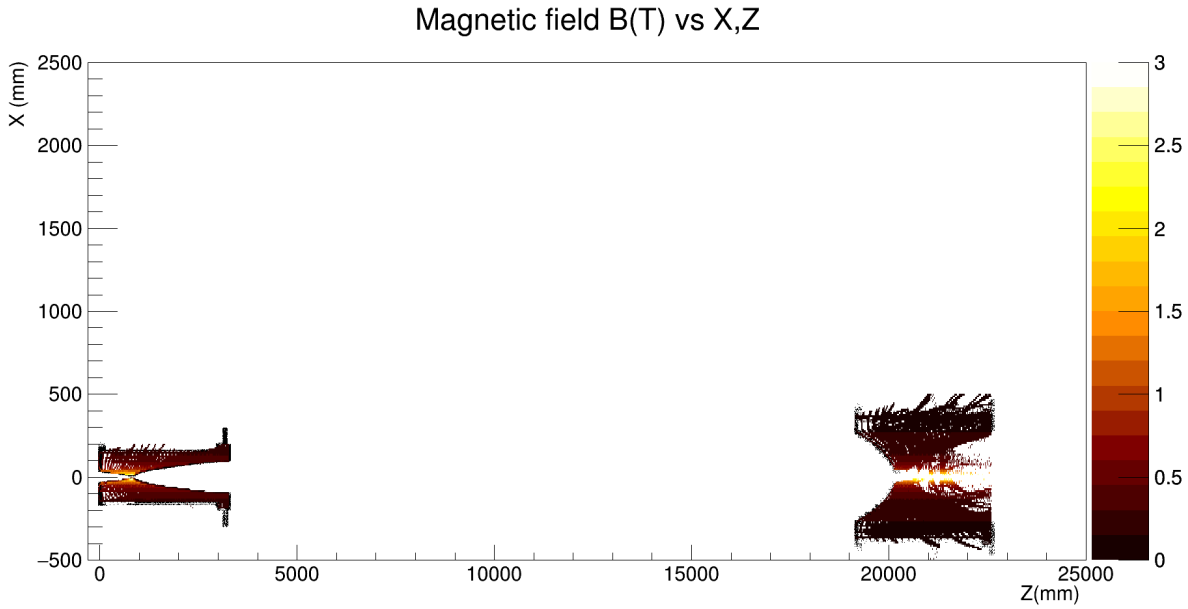

Figure 6.1. Magnetic field for the 2 horns of NuMI beam simulation, not scaled.

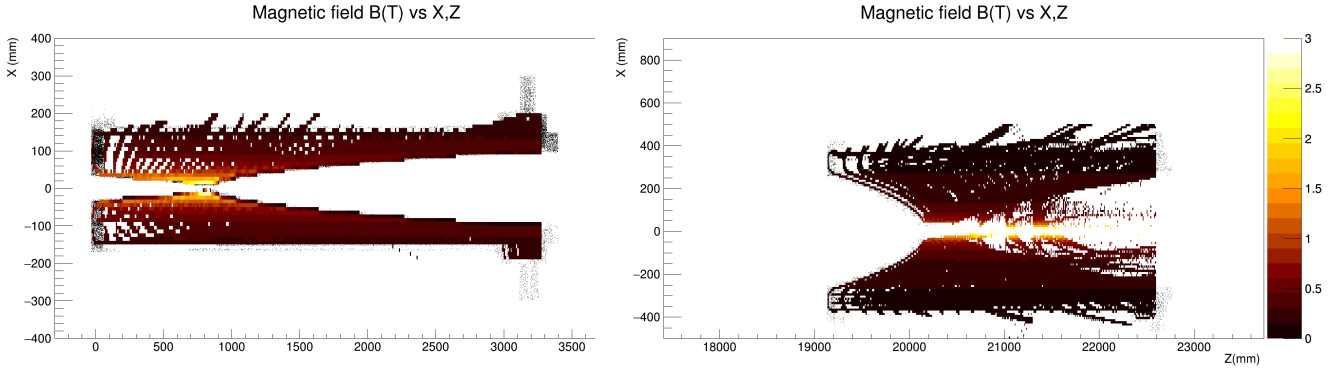

Figure 6.2. Left: Magnetic field in Horn 1 of NuMI beam simulation. Right: Magnetic field in Horn 2 of NuMI beam simulation.

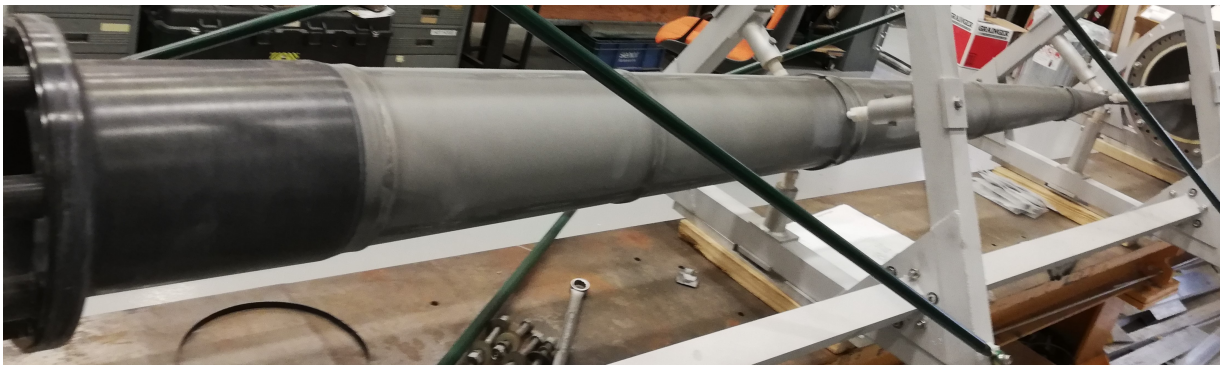

Figure 6.3. Current Equalizer Section in horn 1 (black section on the left).

6.2 CEQ study

As it was described in the section 3.3, the Current Equalizer Section (CEQ) is a straight section used to redistribute the electrical current, see figure 6.3, in the simulation, it is assumed that the current is uniform at the end of the CEQ, when the current comes in to the inner or outer conductor.

In order to study the effect of the CEQ, a simulation by Paul Lebrun [18] and a measurement made by Katsuya Yonehara [35] were made. On the next subsections a comparison between the measurement and CEQ non-symmetrical current distribution and how these distortions modify the flux on the MINERνA detector is described.

6.2.1 Measurement

With the goal to study the magnetic field near to the CEQ, a measurement near to this region was developed by Katsuya within 1% error, the measurement was made on the horn test stand at MI-8.

The magnetic horn 1 has 15 water ports (A, B, C, D, E, F, G, H, I, J, K, L, M, N, O) used as cooling system, water ports from A to O as image 6.4; Katsuya inserted a hall probe with specifications shown on figure 6.5, attached to a support fixed to the outer conductor in two different water ports, L and O, at two different radii from beam axis, 103.0224 mm (near point) and 128.4224 mm (far point), and three different azimuthal angles.

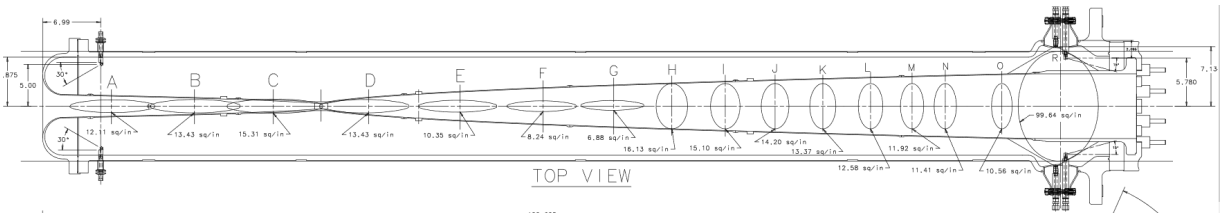

Figure 6.4. Technical drawing for water ports (A, B, C, D, E, F, G, H, I, J, K, L, M, N, O) in horn 1. Image taken from [1].

Z [mm]	R [mm]	B Field [T]
2501	103.022	0.38827
2501	128.422	0.31147
2901	103.022	0.38827
2901	128.422	0.31147

Tabla 6.1: Table with the simulated B field for the two different radii.

Katsuya made 20 sweeps for each horn current (0, 50, 100 and 150 kA) and 40 sweeps for 200 kA, after those measurements, the hall probe was flipped 180 degrees and the measurements was repeated. A weight function was applied to estimate the mean of normalized magnetic field.

The higher uncertainty in the measurement was due to the sensor area, which has an uncertainty of 0.05 inches (1.27 mm) on the radial direction. From the equation 3.1, the field looks like 1/R, the uncertainty depends on the radius where the measurement was made.

The L water ports are at 2532.94 mm from the front of the horn 1, at 2501.06 mm from the MCZERO, the O water ports are at 2934.59 mm from the front of the horn, 2902.71 mm from the MCZERO. There are water ports in three azimuthal directions, at $\pi/2$, $7\pi/6$ and $11\pi/6$ taking the default coordinate system for NuMI beam (Z axis at the same direction to the beamline, X axis the width, and Y axis the height).

The values of the nominal magnetic field are in table 6.1, and the value for the measurements are in table 6.2.

Fast 1-D Hall probe

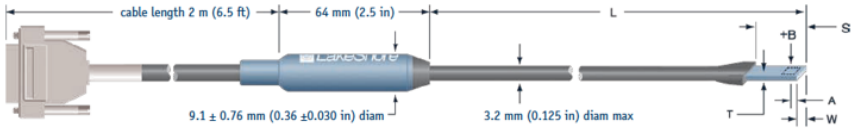

	W (in)	T (in)	A (in)	L (in)	S (in)	Active area (in)	Stem material	Frequency range	Usable full scale ranges	Corrected accuracy (% rdg at 25 °C)	Operating temp range	Temp coefficient (max) zero	Temp coefficient (max) calibration	Contains temp sensor
for Models 475 and 455														
HMFT-3E03-VR	0.135 max	0.025 max	0.125 ±0.005	3 +0.5 -0.125	0.375	0.040 dia (approx)	Flexible plastic tubing	DC to 20 kHz	HSE 3.5 G, 35 G, 350 G, 3.5 kG, 35 kG	±0.20% to 30 kG; ±0.25% 30 to 35 kG	0 °C to +75 °C	±0.09 G/°C	±0.015%/°C	Yes
HMFT-3E03-VF								DC to 800 Hz	HST-4 35 G, 350 G, 3.5 kG, 35 kG	±0.10% to 30 kG; ±0.15% 30 to 35 kG		±0.13 G/°C	–0.005%/°C	
HMFT-2903-VJ	0.085 max	0.020 max	0.065 ±0.005			0.030 dia (approx)		DC to 20 kHz	HSE 3.5 G, 35 G, 350 G, 3.5 kG, 35 kG	±0.50% to 35 kG		±0.09 G/°C	±0.015%/°C	
HMFT-2903-VH								DC to 800 Hz	HST-4 35 G, 350 G, 3.5 kG, 35 kG	±0.25% to 35 kG		±0.13 G/°C	–0.005%/°C	
HMFT-4F15-VR	0.150 ±0.005	0.045 max	0.150 ±0.050	15 ±0.5	0.75	0.040 dia (approx)	Flexible plastic tubing and epoxy fiberglass	DC to 20 kHz	HSE 3.5 G, 35 G, 350 G, 3.5 kG, 35 kG	±0.20% to 30 kG; ±0.25% 30 to 35 kG		±0.09 G/°C	±0.015%/°C	
HMFT-4F15-VR-HF								DC to 50 kHz						
HMFT-4F15-VF								DC to 800 Hz	HST-4 35 G, 350 G, 3.5 kG, 35 kG	±0.10% to 30 kG; ±0.15% 30 to 35 kG		±0.13 G/°C	–0.005%/°C	

Figure 6.5. Specifications for hall probe used to measured the B field. Image taken from [35].

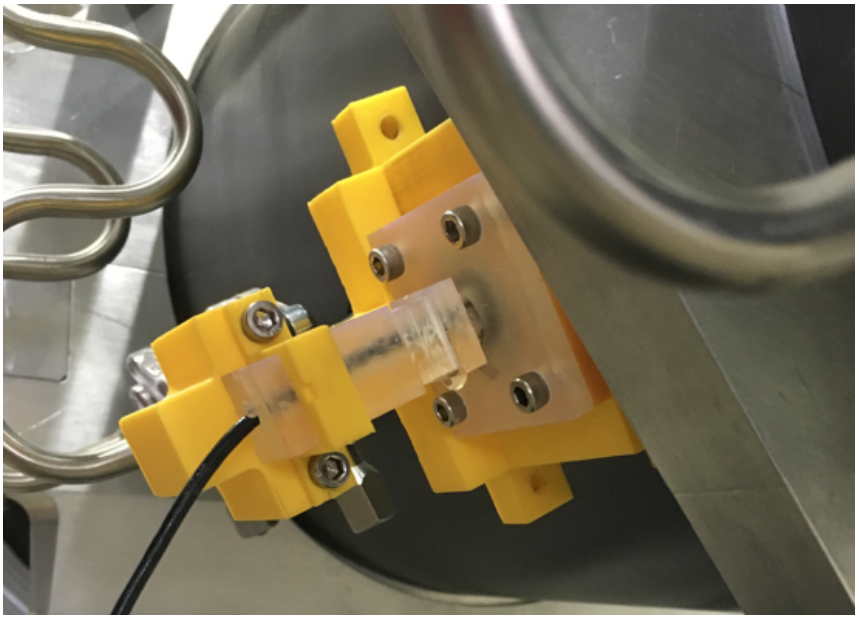

Figure 6.6. Hall probe in a cooling water port to measure the B field. Image taken from [35].

Z [mm]	R [mm]	ϕ	B Field [T]	uncertainty [T]
2501	103.022	$\pi/2$	0.38299	$\pm$ 0.00487
2501	103.022	$7\pi/6$	0.38881	$\pm$ 0.00485
2501	103.022	$11\pi/6$	0.38833	$\pm$ 0.00487
2901	103.022	$\pi/2$	0.38344	$\pm$ 0.00485
2901	103.022	$7\pi/6$	0.38583	$\pm$ 0.00493
2901	103.022	$11\pi/6$	0.38894	$\pm$ 0.00485
2501	128.422	$\pi/2$	0.30718	$\pm$ 0.00310
2501	128.422	$7\pi/6$	0.31064	$\pm$ 0.00320
2501	128.422	$11\pi/6$	0.31044	$\pm$ 0.00319
2901	128.422	$\pi/2$	0.30608	$\pm$ 0.00314
2901	128.422	$7\pi/6$	0.30932	$\pm$ 0.00315
2901	128.422	$11\pi/6$	0.31027	$\pm$ 0.00314

Tabla 6.2: Table with the B field measurements for two Z, two R and three azimuthal positions.

6.2.2 Simulation

The measured points were found on the G4NuMI simulation, four points enclosed in the blue circles of image 6.7. A comparison is presented on the plots 6.8 for the L and O water ports. The χ^2/ndf was obtained using the definition 6.1, this value for the nominal simulation is equal to 0.674. The measurement is consistent with the nominal value of the magnetic field.

$$\chi^2 = \frac{(data - MC)^2}{uncertainty^2} \tag{6.1}$$

Paul developed a study for the CEQ of horn 1 where the current density is not symmetric, the asymmetry electrical current density decreases exponentially, starting at the beginning of the CEQ and decaying upstream of the horn, with a factor called "length scale". A Taylor expansion was included to add quadrupolar terms, where each peak corresponds to the stripline. The magnetic field on the Z direction, beam axis, was omitted.

An example of the asymmetry electrical current density with a quadrupolar term, the length scale and the stripline are shown in the figures 6.9, 6.10 and 6.11.

Different configurations of length scale, from 12.5 to 100, and quadrupolar amplitude were tested, figures 6.12. The χ^2/ndf was obtained; from figures 6.13, it is possible to

see that the configurations more consistent with the measurements are for high length scales and low quadrupolar amplitude. With that information, an increase on the length scale and reductions on quadrupolar amplitudes were applied; the χ^2/ndf was obtained, figure 6.14. A version of this plot with text values is shown on the appendix A.3. The configuration most consistent with the measurement was for length scale equal to 162.5 and quadrupolar amplitude equal to 0.025 with χ^2/ndf equal to 0.502, the comparison between the measurement and the simulation are in A.4.

The flux at the center of the MINERνA detector was produced for each configuration with 1×10^7 POT (Protons On Target). For hadrons and muons with low momentum, 500 MeV/c, there are problems when the tracks in horn 1 are bigger than 6 meters, they cause memory corruption in Root files, those tracks were killed. The energy spectra is not correct for the first 2 bins.

For high length scales, bigger than 75, the simulation is broken in the high energy region, the histogram and the ratio are shown in the plots 6.15 for CEQ with length scale equal to 100 and quadrupolar amplitude equal to 0 (plots for length scale equal to 50, 62.5 and 75 are shown from A.5 to A.7), the comparison between the measurement and the simulation is equal to 6.8. When the quadrupolar amplitude is equal to 0, the flux should be similar to the nominal simulation, the effect disappears, but the flux obtained is very different for high energies, about 100%. The simulation can not be trusted for large CEQ length scales.

The small length scale with smallest χ^2/ndf (0.546) was obtained with CEQ length scale equal to 37.5 and quadrupolar amplitude equal to 0.075, the comparison are in A.8, the ν_μ flux and the ratio of the nominal over CEQ are shown on 6.16. The effect for low and high energies are around 2%, but more statistics are necessary.

6.3 Decay Pipe study

The decay pipe, a pipe of 2 meters of diameter and 675 m of length where the particles decay into neutrinos and muons, has a magnetic field inside. In order to see the effect of this magnetic field on the flux the implementation of the magnetic field on the Geant4 NuMI beam simulation was applied.

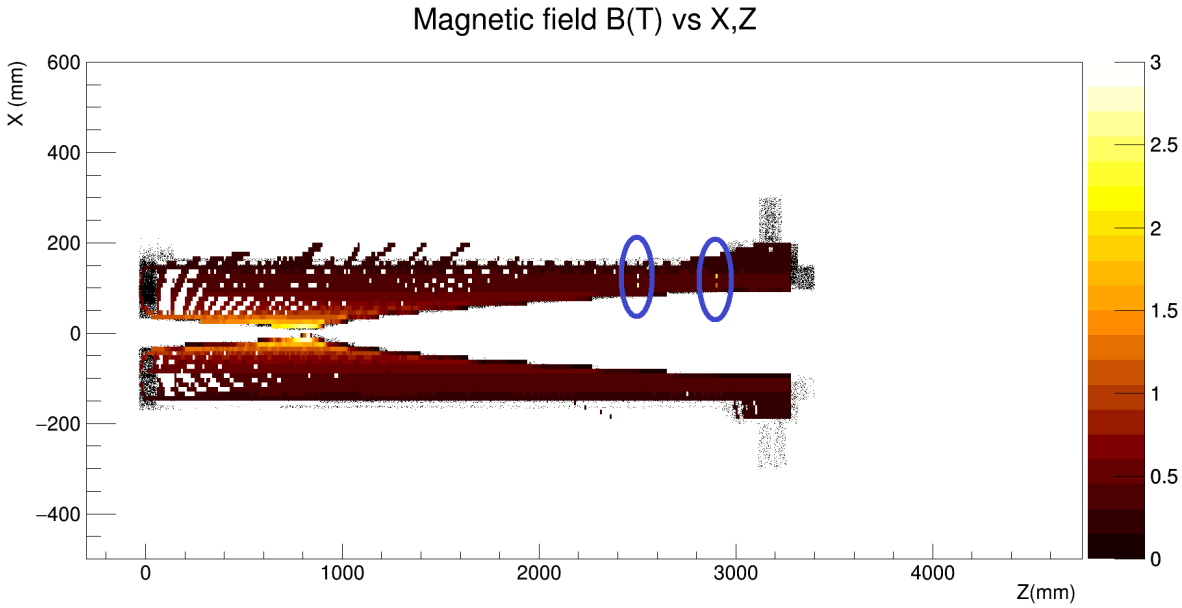

Figure 6.7. Measured points located on the geant4 simulation.

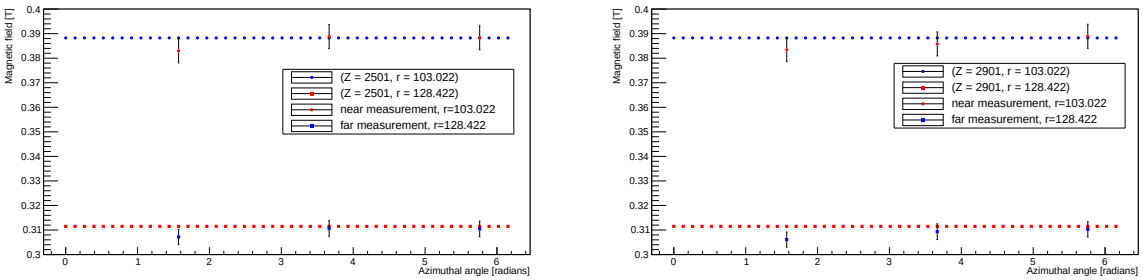

Figure 6.8. Comparison between the measurement and the nominal value for the magnetic field on water port L (left) and O (right).

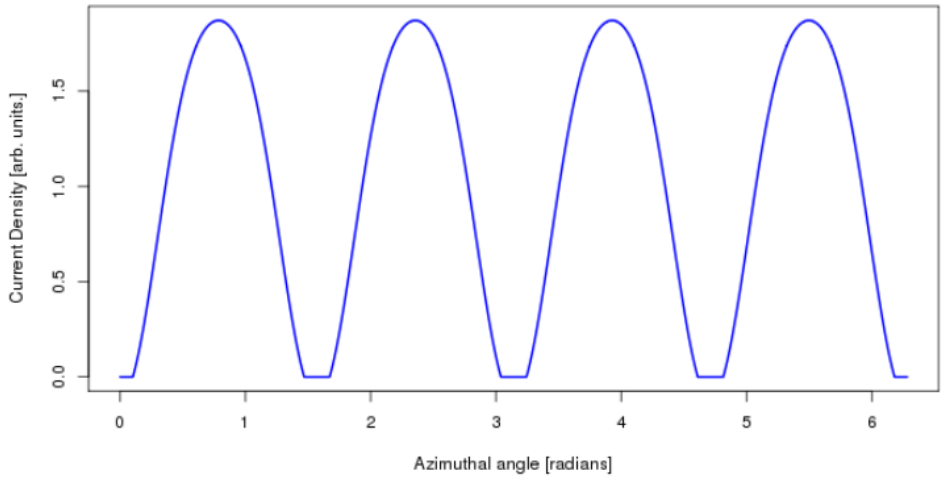

Figure 6.9. Asymmetry electrical current density at the end of horn 1, beginning of CEQ, where each peak corresponds to the stripline. Image taken from [18].

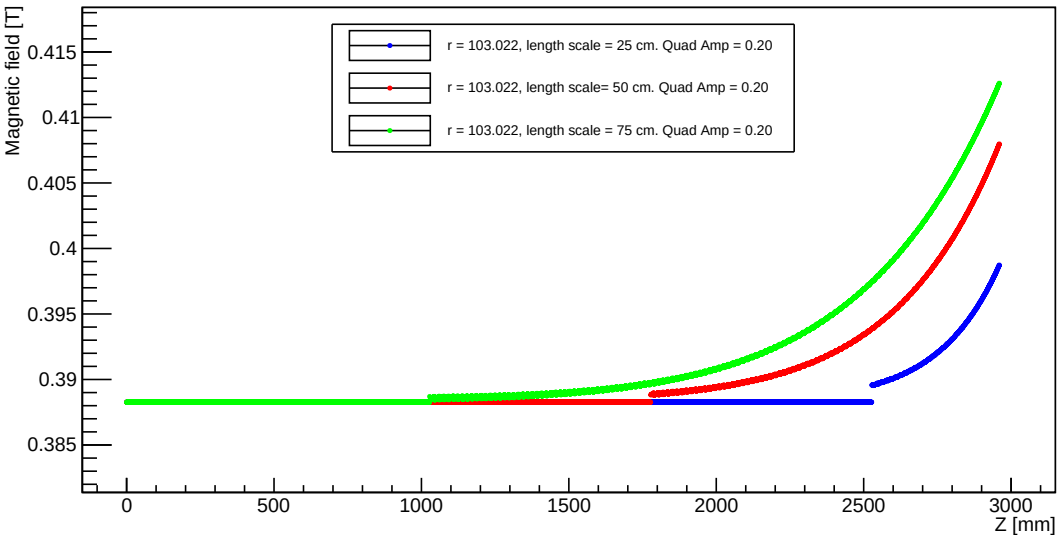

Figure 6.10. Comparison between three different lengths scale values with the same quadrupolar amplitude, at r = 103.022 mm, and $\phi = \pi/4$.

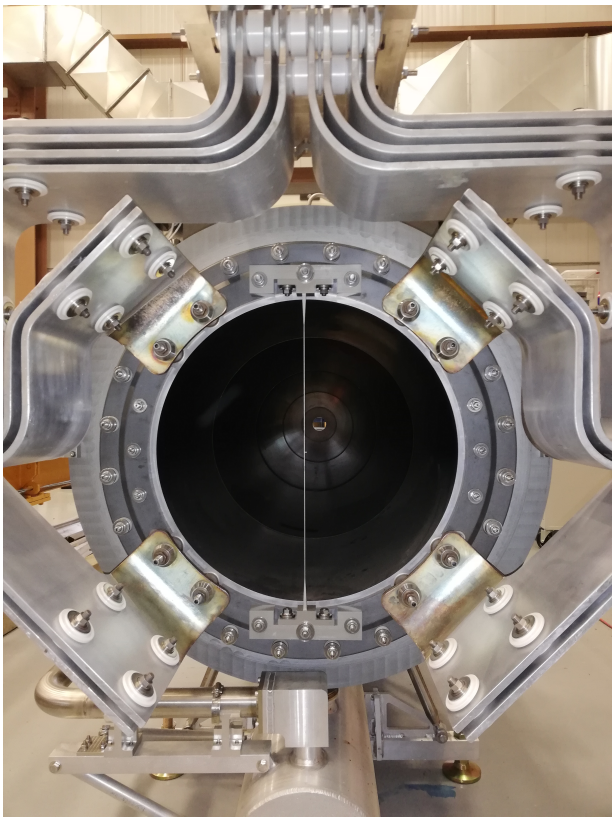

Figure 6.11. Stripline of NuMI horn 2 taken at the MI-8.

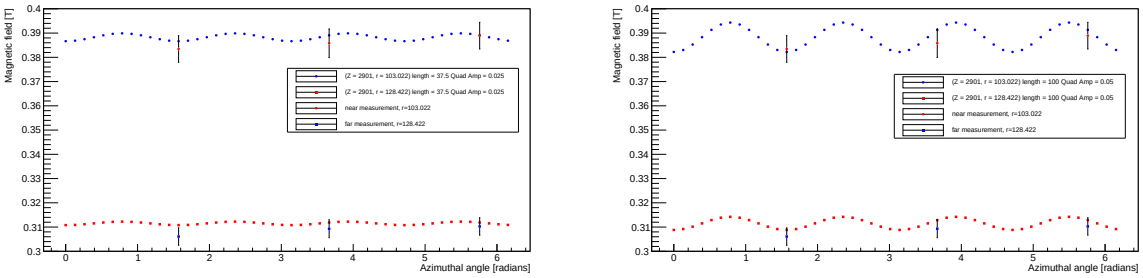

Figure 6.12. Left: comparison between the measurement and length scale = 37.5, quadrupolar amplitude = 0.025 on water port O. Right: comparison between the measurement and length scale = 100, quadrupolar amplitude = 0.05 on water port O.

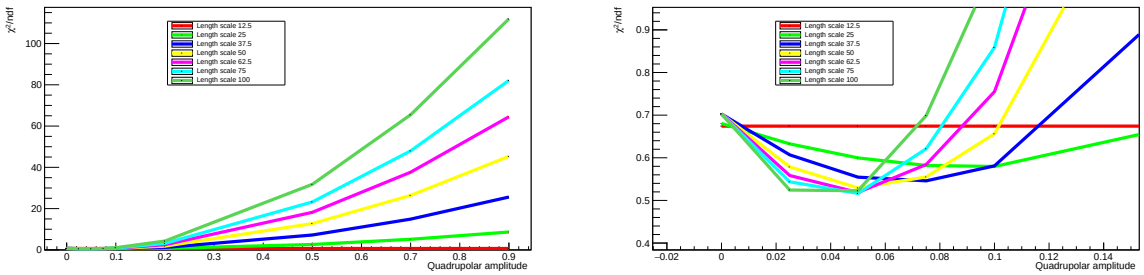

Figure 6.13. χ^2/ndf versus Quadrupolar amplitude for different length scales, the right plot is a zoom for the left plot.

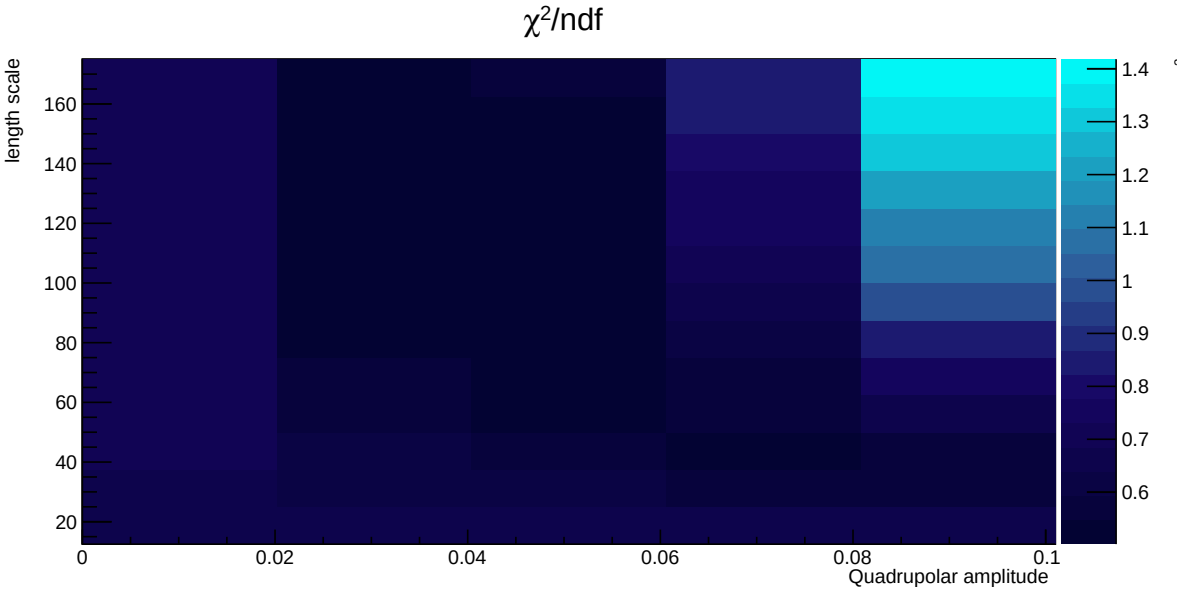

Figure 6.14. χ^2/ndf for different Quadrupolar amplitude and length scales, the darkest zones are the most consistent with the measurement.

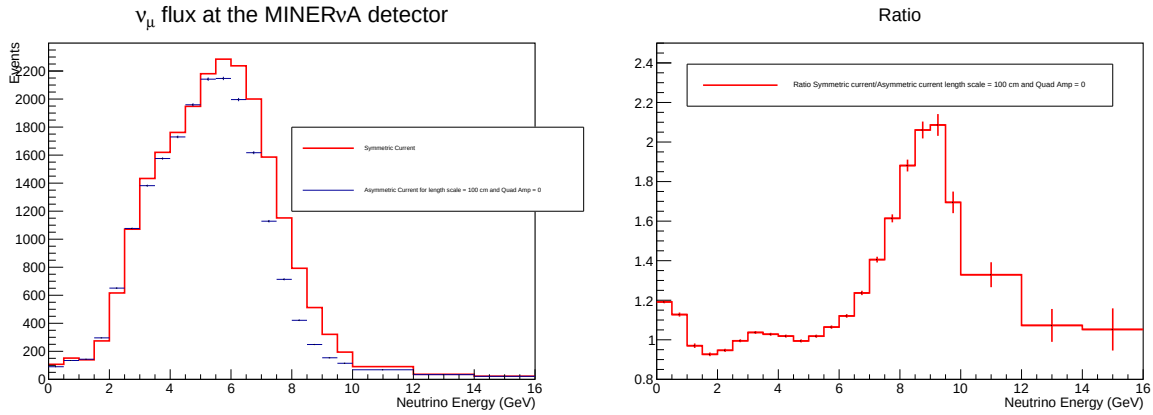

Figure 6.15. Left: Histogram of ν_μ flux at the center of the MINERνA detector, nominal simulation on red, CEQ length scale = 100 and quadrupolar amplitude equal to 0.0 on blue. Right: Ratio of ν_μ flux at the center of the MINERνA detector, nominal simulation over CEQ length scale = 100 and quadrupolar amplitude equal to 0.0.

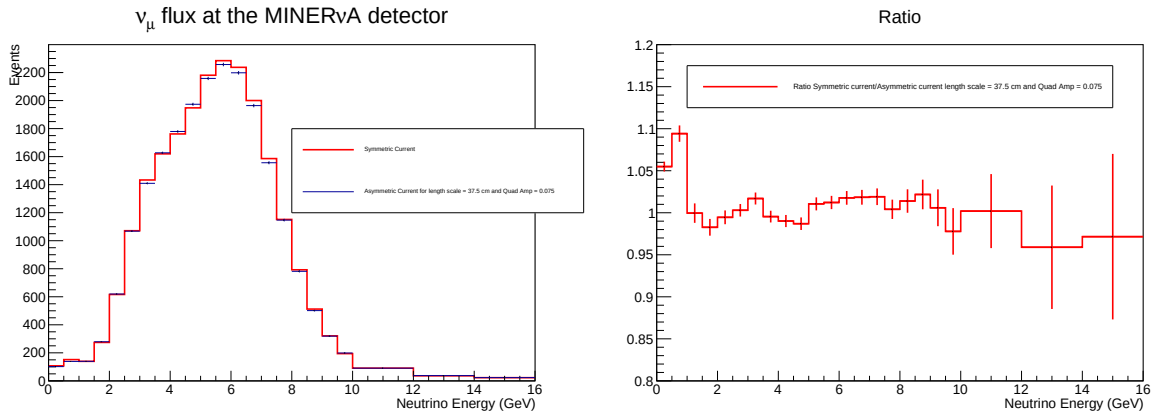

Figure 6.16. Left: Histogram of ν_μ flux at the center of the MINERνA detector, nominal simulation on red, CEQ length scale = 37.5 and quadrupolar amplitude equal to 0.075 on blue. Right: Ratio of ν_μ flux at the center of the MINERνA detector, nominal simulation over CEQ length scale = 37.5 and quadrupolar amplitude equal to 0.075.

The magnetic field was measured on 2003 by Jim Hylen, the average values for the field were $B_x = 0.1$ G, $B_y = -0.3$ G and $B_z = -0.07$ G. The average magnetic field of the Earth is 0.5 G [16]; the field inside of the decay pipe is similar to the Earth magnetic field. In comparison with the magnetic field inside the magnetic horns, between 3 T and 0.1 T, the field is upto 0.0023% on the neck of horn 1, the difference is big but the length of the decay pipe can not be ignored.

A flux comparison between the nominal simulation with and without magnetic field on the decay pipe was done in order to obtain uncertainties that could help on the "wiggle problem". The study was made with neutrino and antineutrino mode, for 1×10^8 POT and horn current equal to 200 kA (-200 kA for antineutrino mode). The flux histogram for neutrino (antineutrino) mode is presented in the left of figure 6.17 (6.18), where the nominal simulation, magnetic field off, is on blue color, and the simulation with magnetic field on decay pipe, is on red color. The ratio between magnetic field on over off is presented on the right.

The effect for neutrino mode for energies between 6 to 9 GeV is around 3%, when the magnetic field on decay pipe is turned on, the number of particles is reduced, for low energies there are no changes. In antineutrino mode, the biggest change, is around 2% for high energies between 7 and 9 GeV. The number of events when the magnetic field is turned on increases, opposite to the neutrino mode, which is reasonable, hence the magnetic force is in opposite direction for each configuration. There are 2 fluctuations around 1% for low energy, 1.5 and 5 GeV, more statistics could help to understand those bins.

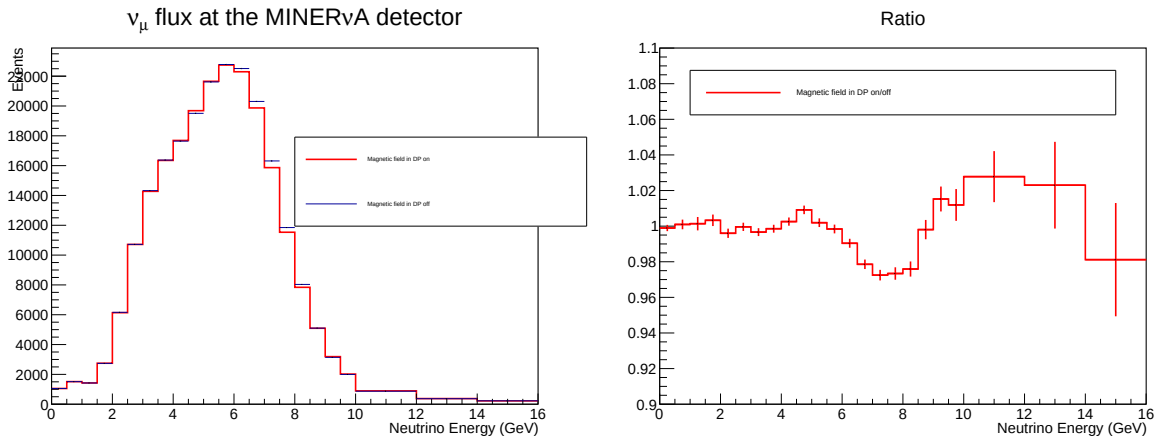

Figure 6.17. Left: ν_μ flux at the center of the MINERνA detector, the red one corresponds to magnetic field on, and the blue one to magnetic field off. Right: Ratio of ν_μ flux at the center of the MINERνA detector, magnetic field ON/OFF on decay pipe. Obtained with the nominal simulation of NuMI beam on Geant4.

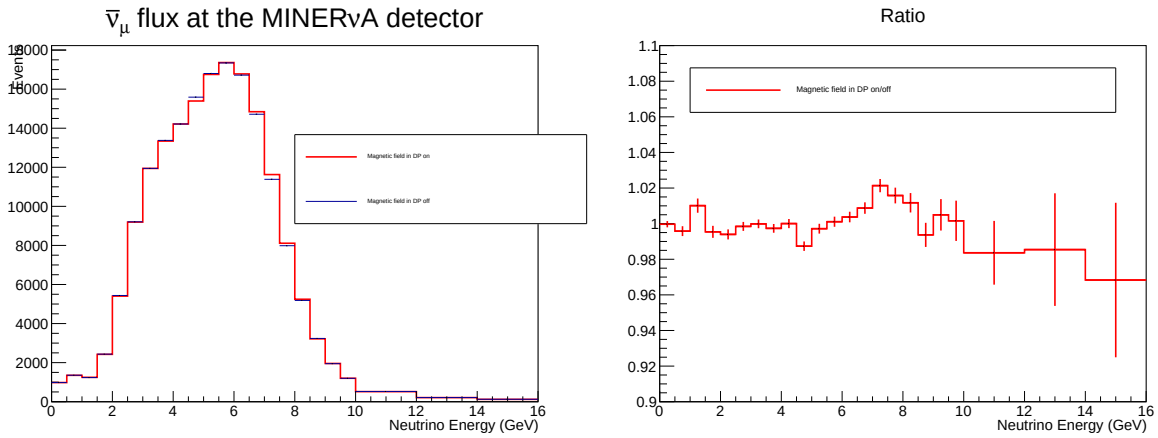

Figure 6.18. Left: $\bar{\nu}_\mu$ flux at the center of the MINERνA detector, the red one corresponds to magnetic field on, and the blue one to magnetic field off. Right: Ratio of $\bar{\nu}_\mu$ flux at the center of the MINERνA detector, magnetic field ON/OFF on decay pipe. Obtained with the nominal simulation of NuMI beam on Geant4.

Chapter 7. LBNF studies

The design for the optical system on LBNF is in progress; studies on the design for magnetic horns are under development; changes on the thickness of the inner conductor and the design of drain holes are examples of variable under consideration. In this chapter the design and the impact on the flux due to the four drain holes on horn A are described.

7.1 Drain hole simulation on ANSYS

The magnetic horns have 4 drain holes, see pictures 7.1, the diameter of the drain holes for horn A of LBNF is equal to 101.6 mm; a distortion on the magnetic field should be studied to understand the effect of that holes on the neutrino flux. Zhijing made a simulation of the magnetic field near to the drain holes [36] using Maxwell 3D of ANSYS [2].

He took a quarter of the horn with a horn current equal to 75 kA, see figure 7.2. The coordinate system used on the ANSYS simulation is different that the system used in Geant4 simulation, the X axis is on the direction of the beam (Z axis for Geant4 simulation). The "r" and "ϕ" axis are the same for Geant4 simulation. The inner radius of outer conductor is equal to 220.5 mm, but the simulation was made with the highest radius of 210.0 mm.

The simulation is presented in figure 7.3. The nominal simulation only has magnetic field on polar direction (ϕ component) that goes like 1/R. The magnetic field for drain holes has components in the R and Z directions. The magnetic field simulation is presented as points on a grid, figure 7.4, with steps of 9 degrees on angular component ϕ. Steps of 5 mm on Z direction from the center of the hole to 200 mm downstream and upstream. Steps of 20 mm on radial direction from 110 to 210 mm. The relative magnetic field, equation 7.1, for the three components of magnetic field are presented from figures 7.6 to 7.11 where B_{DH} represents the component of the B field with drain holes, B_{Nom} is the component of the nominal B field and B_{Total} is the ideal value of the B field $B = 60/R$.

$$\frac{(B_{DH} - B_{Nom})}{B_{Total}}. \tag{7.1}$$

Figure 7.1. Left: picture of horn 1 outer conductor of NuMI beam, only 3 visible drain holes on the image. Right: drain holes on horn 2 of NuMI beam, only the bottom drain hole is used to drain water and gas, a pump is used to drain to a water tank to process and reuse the fluids, the 3 remaining drain holes are used as input of water and gas (Argon for NuMI).

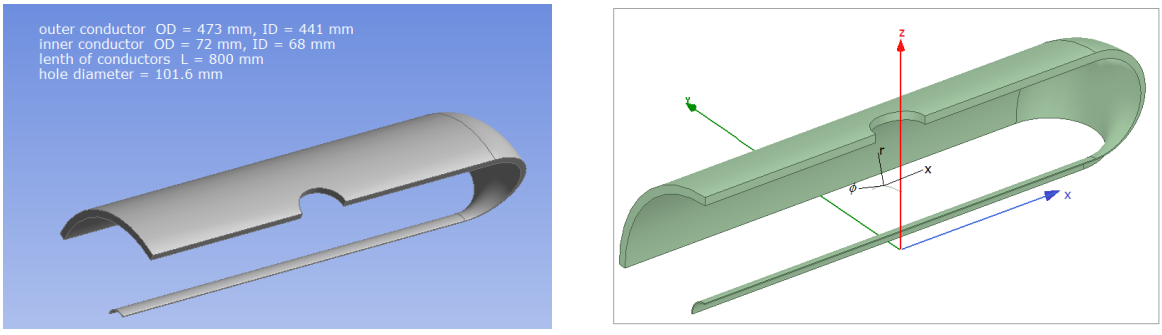

Figure 7.2. Left: a quarter of horn A of LBNF simulated on ANSYS, the hole diameter equal to 101.6 mm. Right: Coordinate system for ANSYS simulation, the coordinate system is different that the used for Geant4 simulation. Images taken from [36].

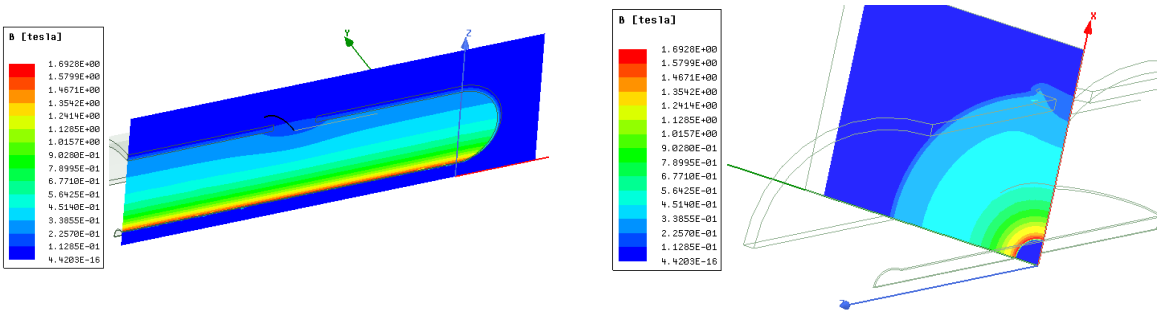

Figure 7.3. Drain hole magnetic field simulation on ANSYS presented by Zhijing, the magnetic field goes from 1.69 T to 0.11 T. Image taken from [36].

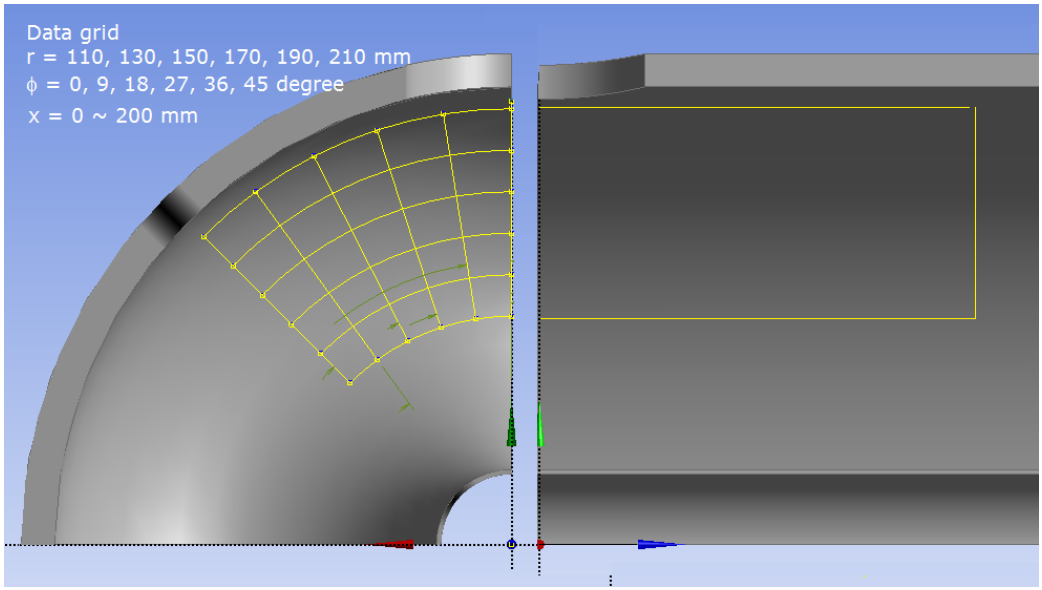

Figure 7.4. The grid was made with steps of 9 degrees on angular component ϕ. Steps of 5 mm on Z direction from the center of the hole to 200 mm downstream and upstream. Steps of 20 mm on radial direction from 110 to 210 mm. Image taken from [36].

7.2 Drain hole simulation on GEANT4

To reproduce the magnetic field of drain holes, a field map was created with three components of magnetic field. The magnetic field for drain holes was made using the grid of ANSYS point and a SPLINE function on ROOT, figure 7.5, where the interpolation was made using the six steps of 20 mm on R, 110 to 210 mm, the interpolation was made for the three components of B field, for angles between -45 to 45 degrees with steps of 9 degrees and 81 steps of 5 mm on beam axis centring on the hole center. The last interpolation is only for one drain hole, the four drain holes were simulated on Geant4 LBNF simulation with the nominal B field for the rest of the horn A. The comparison between the ANSYS and the Geant4 simulation is presented in the pictures 7.6 to 7.11. It is possible to see the similitudes between the ANSYS and the Geant4 simulations.

The four drain holes was added to the Geant4 simulation and a new parameter to modify the percentage effect of the drain holes was defined; the goal was to see the effect of the distortion on the neutrino flux. To compare the drain holes effect on the neutrino flux, a flux with the default B field, $B = 60/R$, using a field map was produced (percentage effect of drain holes equal to zero). The neutrino flux histograms and ratio for nominal simulation and nominal with field map are shown in 7.12, all the fluxes were produced with 1.5×10^8 POT. The discrepancy between the neutrino flux produced with field map and the nominal is less than 1%. This discrepancy is produced by a shift on the inner electrical conductor radius. To reduce that, steps on R for field map need to be smaller, but it requires more memory when the neutrino flux is produced. The decision taken was to use this step size, the goal is to understand the effect of the drain holes, not the reconstruction of the default B field.

The flux produced with field map using the nominal B field was taken as the default flux. The flux produced with drain holes effect is shown in figure 7.13. The effect of drain holes on the flux is less than 0.5%, basically the drain holes do not have effect on the ν flux. A test with the drain holes effect at 200% bigger was made to see if it modifies the neutrino flux. The plots of the relative B field at 200% are shown in A.9 and A.10. The comparison between the flux with drain holes effect at 200% and the produced with nominal B field is presented in figure 7.14. The effect is still less than 0.5%.

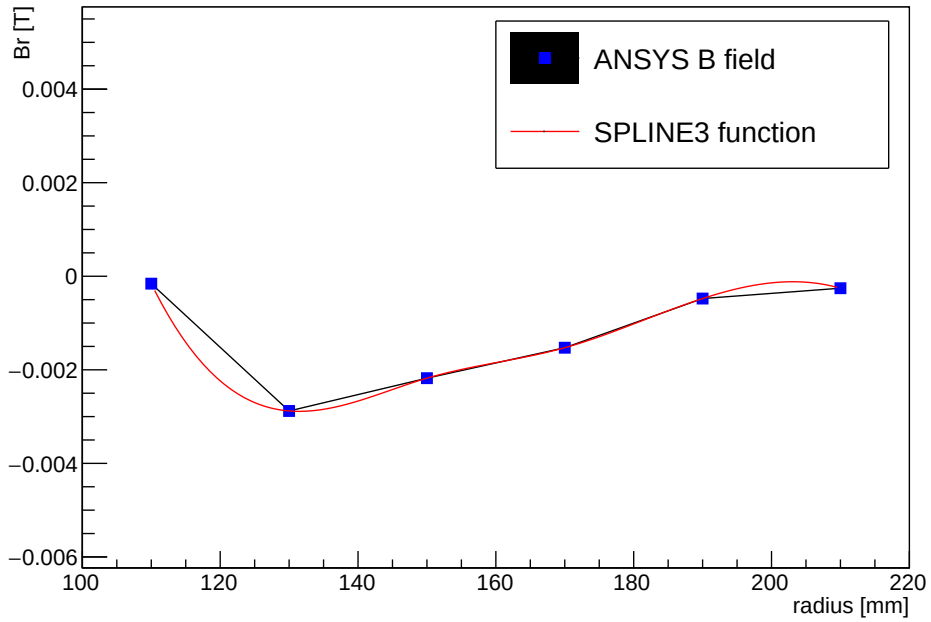

Figure 7.5. Spline function to reproduce the B field, the blue squares are the ANSYS points, the red line is the spline function to make the interpolation between the ANSYS points. This plot is the interpolation for B_r between r equal to 110 to 210 mm.

To make sure that the field map modifies the flux, a deeper effect was tested, the idea is to use the same drain holes effect for small radii. Change of effect from 110 to 210 mm with steps of 20 mm to an effect from 60 to 210 mm with steps of 30 mm. The B field is bigger for small radii, distortions for bigger magnetic fields should modify more the ν flux. The comparison between the relative B field for drain holes effect and the deeper effect are shown on A.11. The comparison between the flux with deep effect and the nominal B field is presented in 7.15, it is possible to see a bigger effect, around 10 times bigger than the drain holes effect (2% over the nominal B field flux) for high energy neutrinos, between 3.5 and 4.5 GeV.

The study for horns B and C was not made because the drain holes only modifies the magnetic field near to the outer conductor, the outer conductor radius for horn A is equal to 220.5 mm with a magnetic field equal to 0.27 T. The outer electrical conductor for horns B and C is equal to 650 mm, the B field near to the outer electrical conductor is less than 0.10 T; distortions on B field, magnetic force, would be smaller in consequence the effect on the ν flux should be smaller.

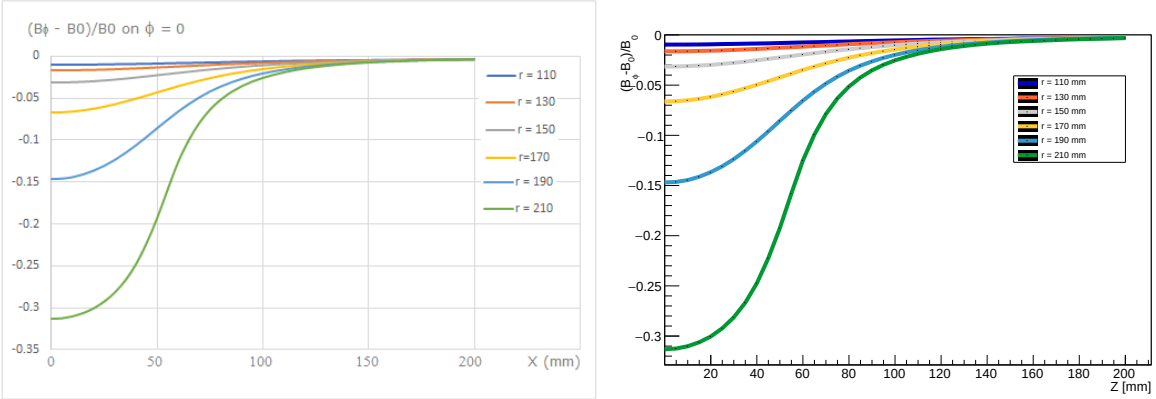

Figure 7.6. Left: relative magnetic field for B_{phi} with an angle of 0 degrees obtained with ANSYS simulation, image taken from [36]. Right: relative magnetic field for B_{phi} with an angle of 0 degrees obtained with Geant4 simulation. In both plots the X axis represents the beam axis (Z), where the zero is the center of the drain hole.

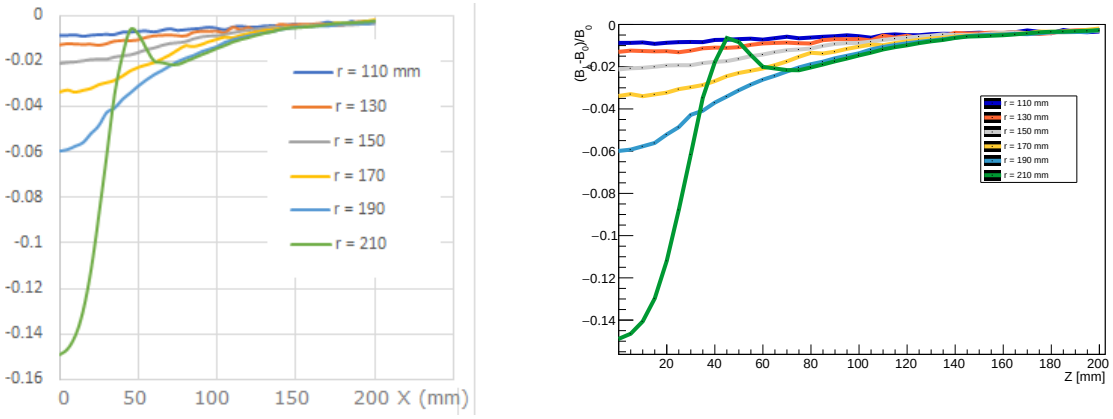

Figure 7.7. Left: relative magnetic field for B_{phi} with an angle of 9 degrees obtained with ANSYS simulation, image taken from [36]. Right: relative magnetic field for B_{phi} with an angle of 9 degrees obtained with Geant4 simulation. In both plots the X axis represents the beam axis (Z), where the zero is the center of the drain hole.

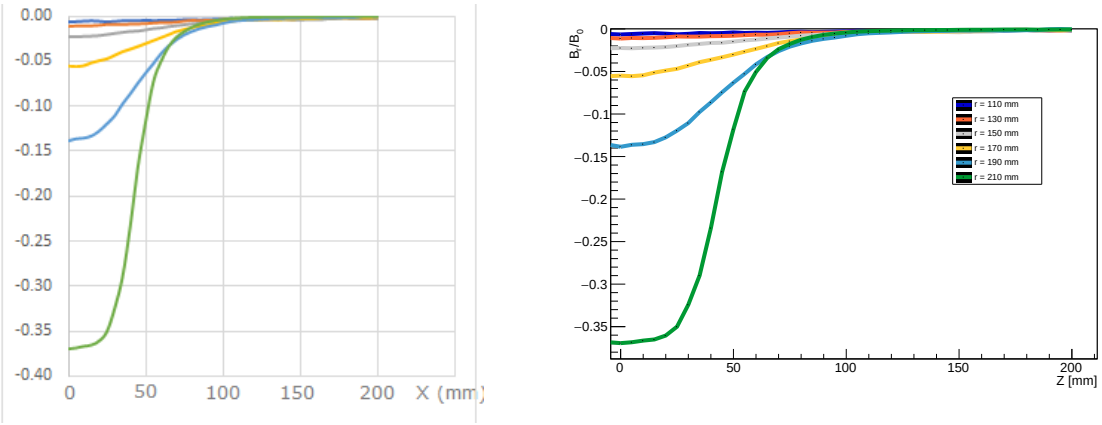

Figure 7.8. Left: relative magnetic field for B_r with an angle of 9 degrees obtained with ANSYS simulation, image taken from [36]. Right: relative magnetic field for B_r with an angle of 9 degrees obtained with Geant4 simulation. In both plots the X axis represents the beam axis (Z), where the zero is the center of the drain hole.

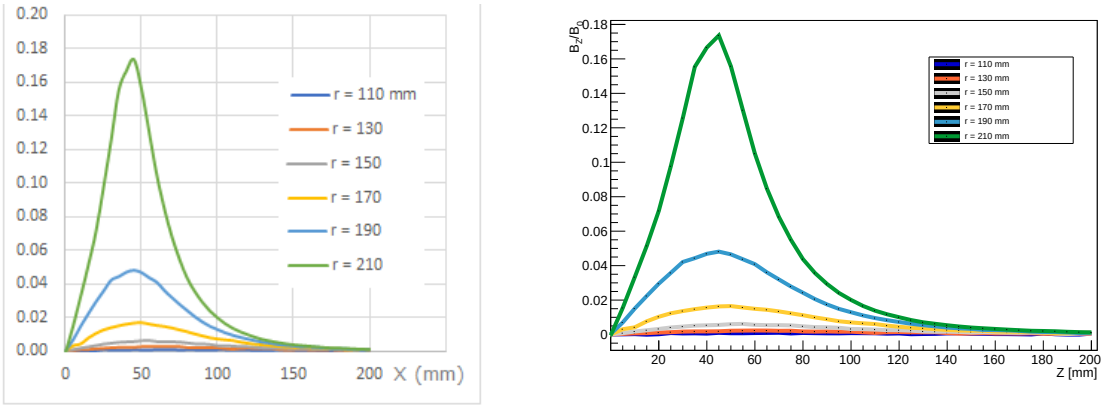

Figure 7.9. Left: relative magnetic field for B_z with an angle of 9 degrees obtained with ANSYS simulation, image taken from [36]. Right: relative magnetic field for B_z with an angle of 9 degrees obtained with Geant4 simulation. In both plots the X axis represents the beam axis (Z), where the zero is the center of the drain hole.

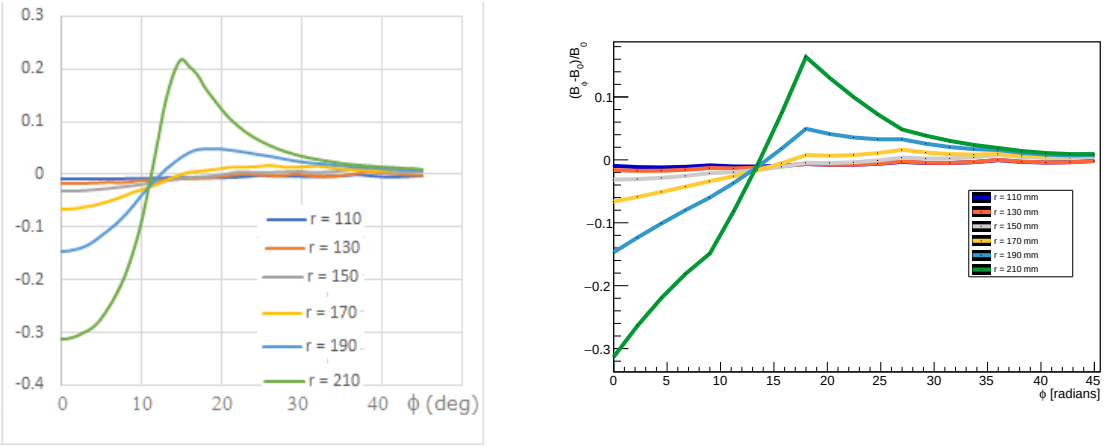

Figure 7.10. Left: relative magnetic field for B_{phi} at the center of drain hole obtained with ANSYS simulation, image taken from [36]. Right: relative magnetic field for B_{phi} at the center of drain hole obtained with Geant4 simulation. In both plots the X axis represents the angle between the radial component and the center of hole.

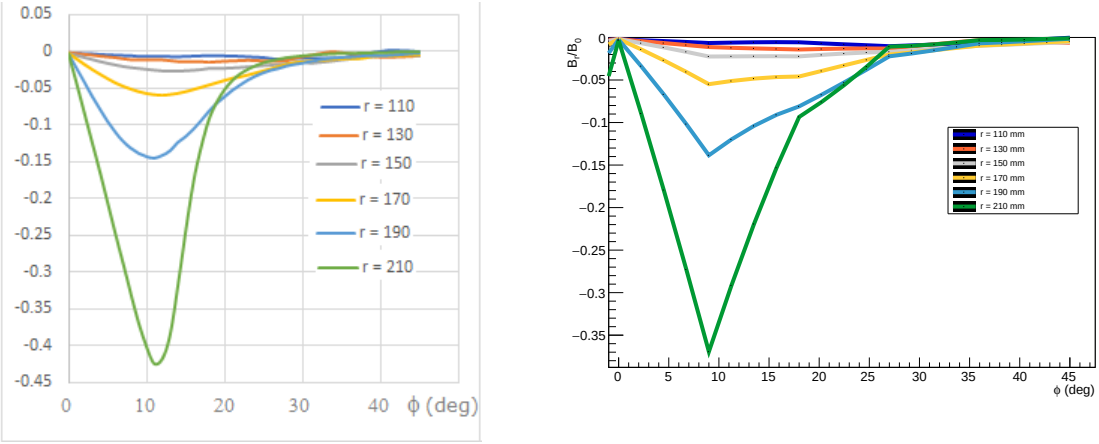

Figure 7.11. Left: relative magnetic field for B_r at the center of drain hole obtained with ANSYS simulation, image taken from [36]. Right: relative magnetic field for B_r at the center of drain hole obtained with Geant4 simulation. In both plots the X axis represents the angle between the radial component and the center of hole.

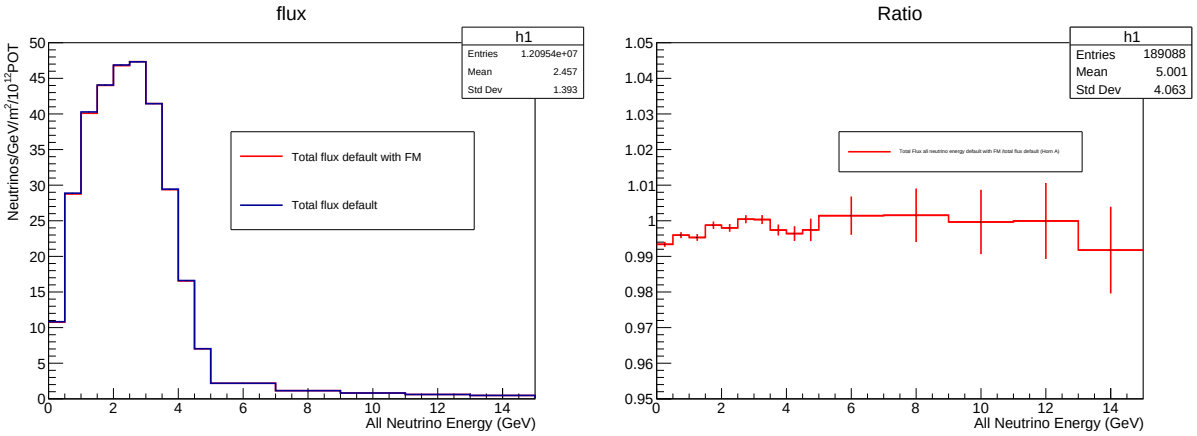

Figure 7.12. Left: Histograms of total ν flux at the DUNE far detector, in red the flux with field map using nominal B field, in blue the flux with nominal simulation. Right: Ratio between the flux with field map using nominal B field over the flux with nominal simulation.

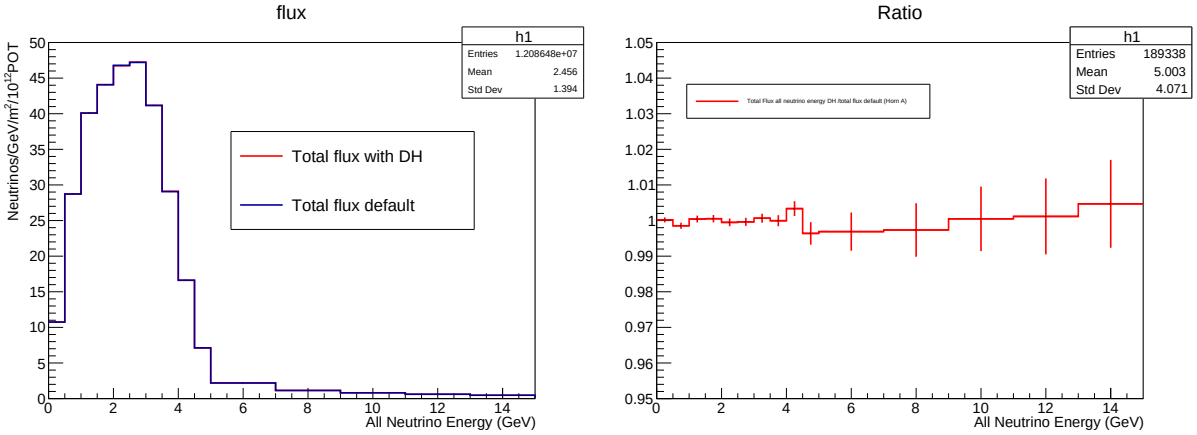

Figure 7.13. Left: Histograms of total ν flux at the DUNE far detector, in red the flux with drain holes, in blue the flux with nominal B field. Right: Ratio between the flux with drain holes over the flux with nominal B field.

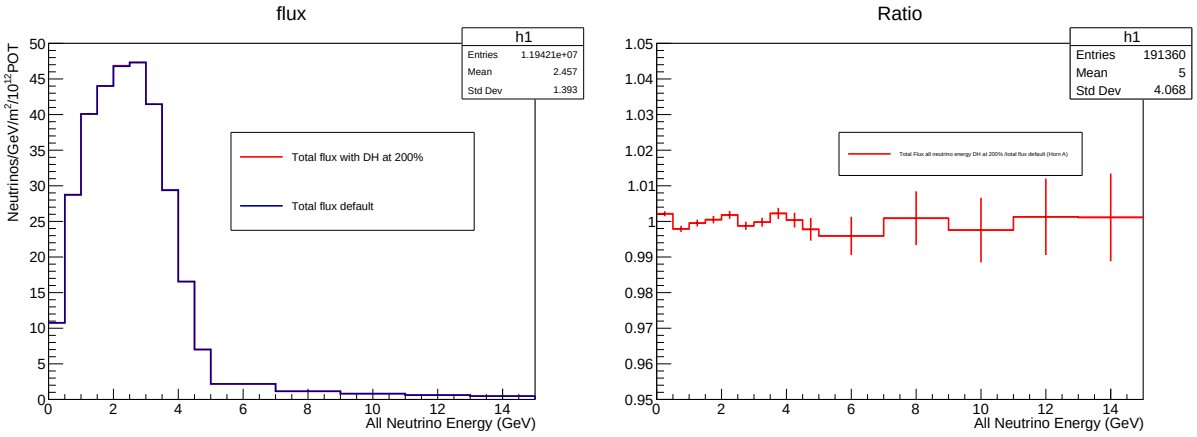

Figure 7.14. Left: Histograms of total ν flux at the DUNE far detector, in red the flux with drain holes at 200%, in blue the flux with nominal B field. Right: Ratio between the flux with drain holes at 200% over the flux with nominal B field.

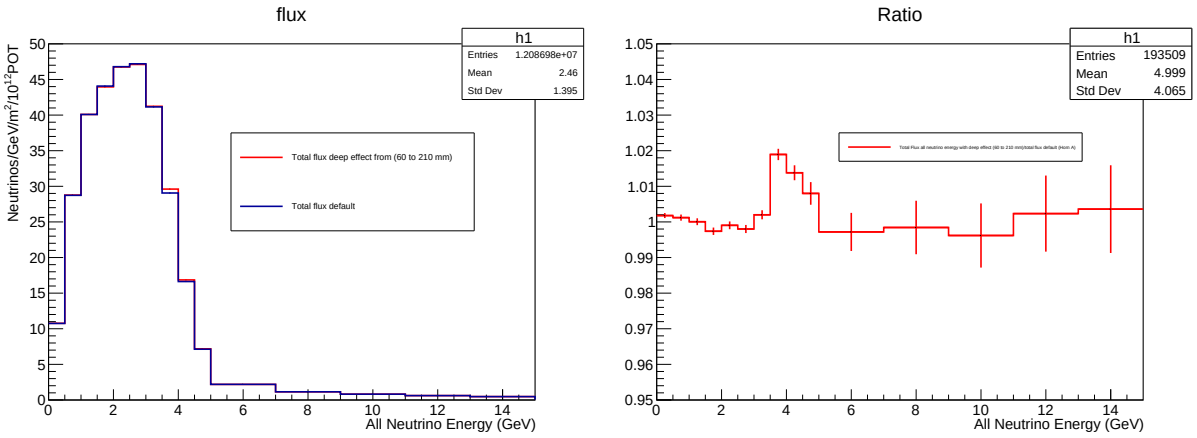

Figure 7.15. Left: Histograms of total ν flux at the DUNE far detector, in red the flux with deeper drain holes effect, in blue the flux with nominal B field. Right: Ratio between the flux with deeper drain holes effect over the flux with nominal B field.

Chapter 8. Conclusions

The neutrinos are one of the most mysterious particles of the universe, the physicists have the task to understand them. One of the first steps is to simulate processes and compare it with data. This simulations needs to be very accurate with a very good understanding of uncertainties. One of the main goals of this work is to understand some of these uncertainties on the focusing systems for NuMI beam and LBNF.

In NuMI beam, studies for magnetic field on CEQ and decay pipe were made. With the CEQ study, a comparison between data and MC was made. We obtain that non uniform electrical current distributions could modify the flux around 3% with configurations more consistent with the measurements than the nominal simulation. But the configurations with smaller χ^2 are broken, a debug of the code and more tests are necessary, including the study for antineutrinos. The magnetic field on the decay pipe modifies the flux in 2% or 3% is a non-negligible uncertainty and it is present in all run of NuMI beam. At the beginning of the study, the goal was to understand the wiggle problem, it was completely accomplished. The MINERνA collaboration found that corrections on the muon energy reconstruction at the MINOS detector remove the wiggle effect, studies are still in progress.

With drain holes results for horn A on LBNF, it is possible to conclude that the field map for drain holes has an impact on the flux of less that 0.5%. The code for drain holes was added to the default LBNF simulation for future works. This result helps to understand the current design for drain holes, which does not modifies the neutrino flux and could be used as the final design; the optimized design is not finished yet but this result helps on that hard task.

The work presented in this thesis was developed at Fermilab as part of the MINERνA collaboration with the goal to understand mismodeling effects on neutrino beam simulations; successful results were obtained. This work will help to MINERνA understand a discrepancy in the neutrino energy spectra in Data and Monte Carlo, and this will also improve the design and the accuracy of the LBNF simulation.

Appendix A. Supplementary plots

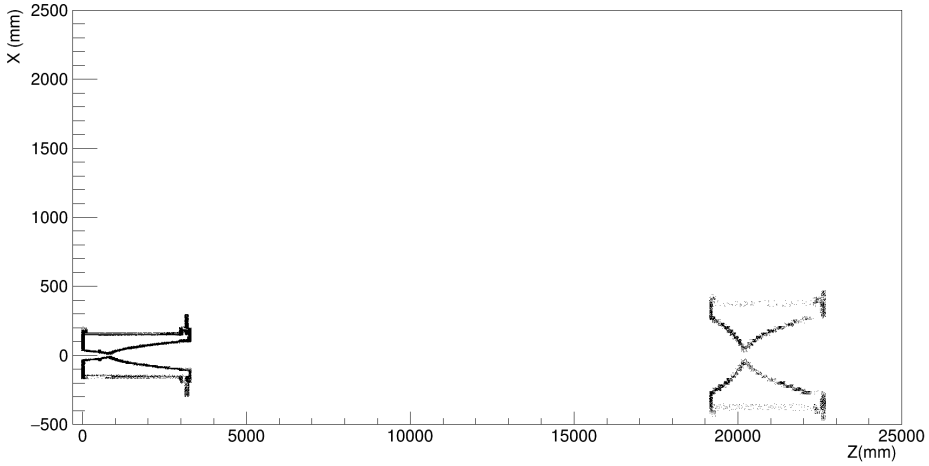

Figure A.1. Shape for the 2 horns of NuMI beam simulation, not scaled. Obtained with Geantinos.

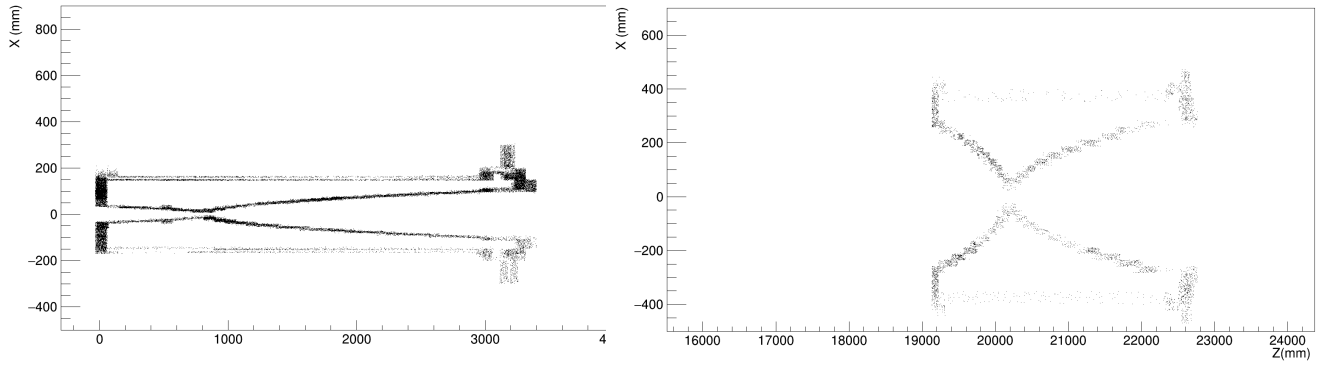

Figure A.2. Left: Horn 1 of NuMI beam simulation. Right: Horn 2 of NuMI beam simulation. Not scaled, obtained with Geantinos.

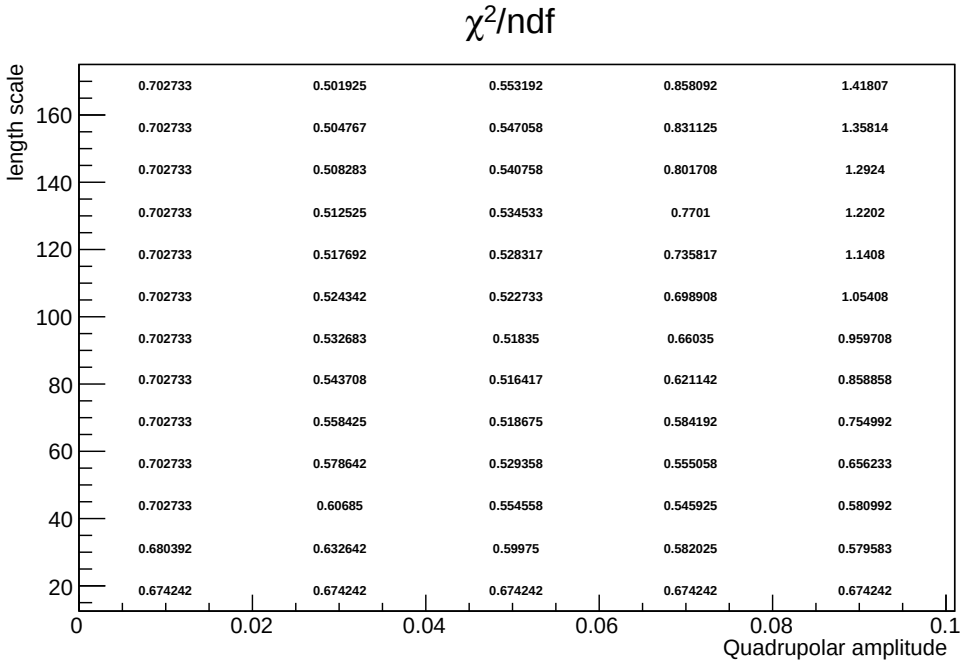

Figure A.3. χ^2/ndf for different Quadrupolar amplitude and length scales, text version, goes from 0.0 to 0.10 with steps of 0.025 on quadrupolar amplitude, and 12.5 to 162.5 with steps of 12.5 on length scale.

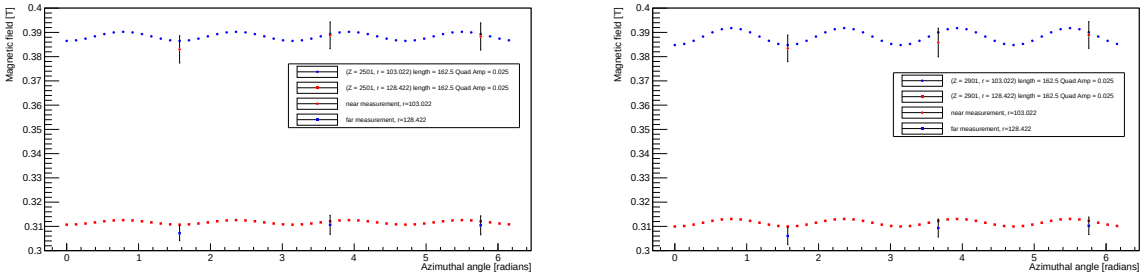

Figure A.4. Comparison between the measurement and length scale = 162.5, quadrupolar amplitude = 0.025 on water port L (left) and water port O (right).

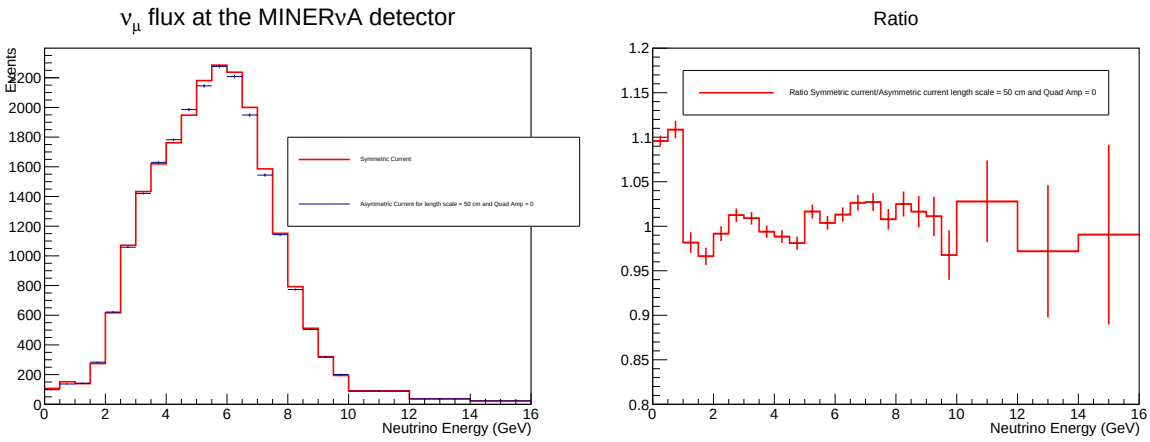

Figure A.5. Left: Histogram of ν_μ flux at the center of the MINERνA detector, nominal simulation on red, CEQ length scale = 50 and quadrupolar amplitude equal to 0.0 on blue. Right: Ratio of ν_μ flux at the center of the MINERνA detector, nominal simulation over CEQ length scale = 50 and quadrupolar amplitude equal to 0.0. The effect for high length scales is not visible, the simulation works for this length scale.

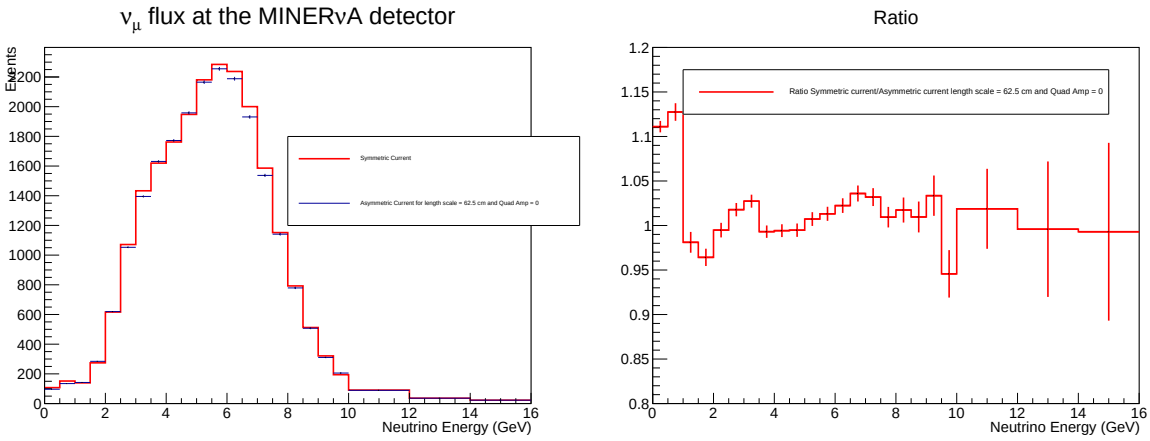

Figure A.6. Left: Histogram of ν_μ flux at the center of the MINERνA detector, nominal simulation on red, CEQ length scale = 62.5 and quadrupolar amplitude equal to 0.0 on blue. Right: Ratio of ν_μ flux at the center of the MINERνA detector, nominal simulation over CEQ length scale = 62.5 and quadrupolar amplitude equal to 0.0. The change from length scale equal to 50 and length scale equal to 62.5 is visible, the simulation starts to brake.

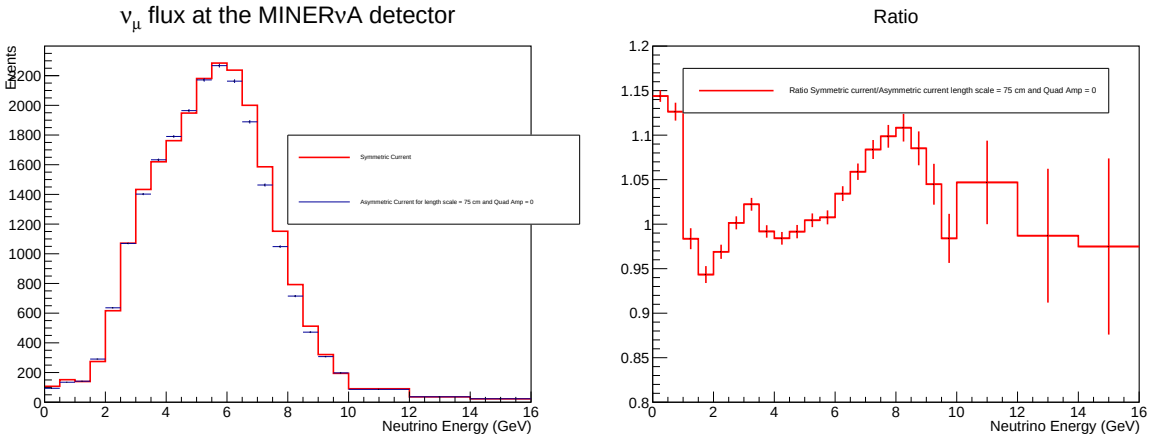

Figure A.7. Left: Histogram of ν_μ flux at the center of the MINERνA detector, nominal simulation on red, CEQ length scale = 75 and quadrupolar amplitude equal to 0.0 on blue. Right: Ratio of ν_μ flux at the center of the MINERνA detector, nominal simulation over CEQ length scale = 75 and quadrupolar amplitude equal to 0.0. The simulation is broken, can not be trusted for this length scale.

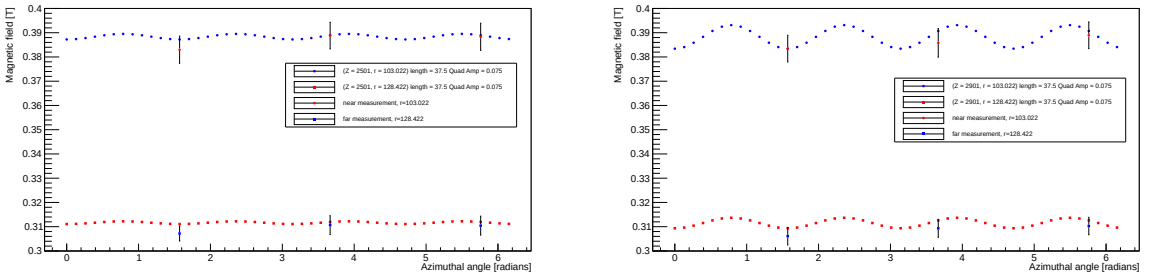

Figure A.8. Comparison between the measurement and length scale = 37.5, quadrupolar amplitude = 0.075 on water port L (left) and water port O (right).

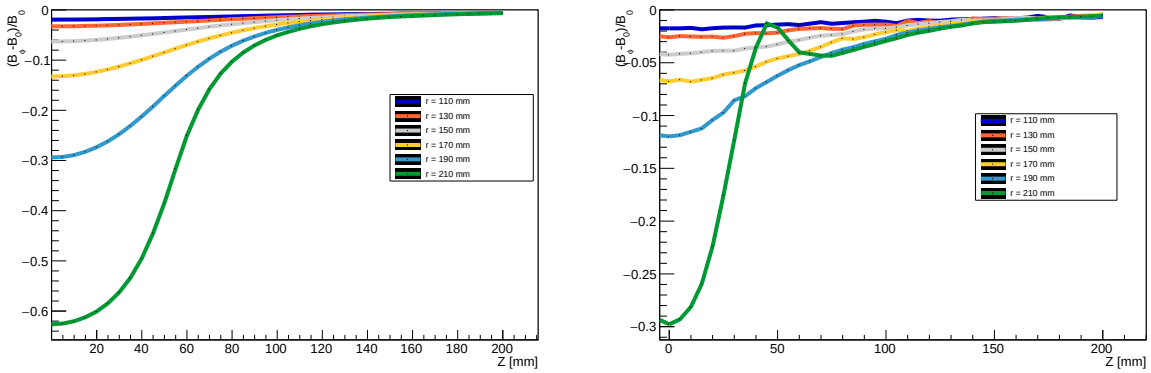

Figure A.9. Left: relative magnetic field for B_ϕ with an angle of 0 degrees with a drain holes effect at 200%. Right: relative magnetic field for B_ϕ with an angle of 9 degrees with a drain holes effect at 200%. In both plots the X axis represents the beam axis (Z), where the zero is the center of the drain hole.

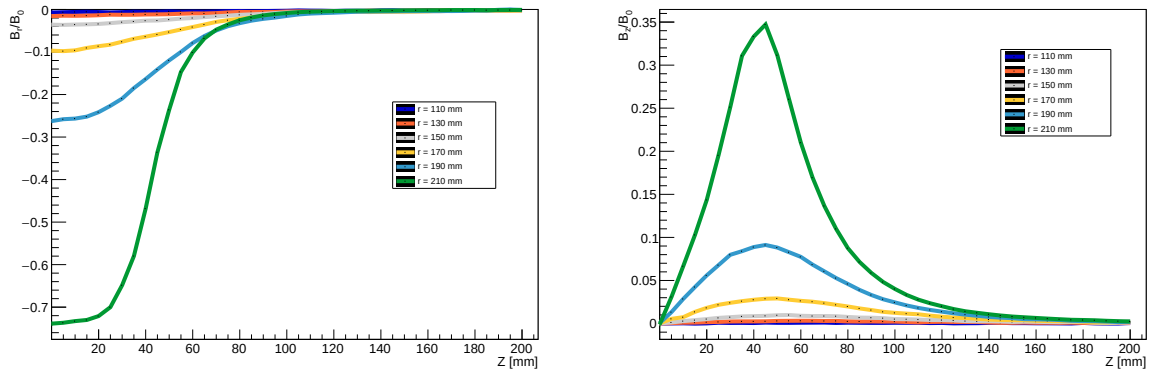

Figure A.10. Left: relative magnetic field for B_r with an angle of 9 degrees with a drain holes effect at 200%. Right: relative magnetic field for B_z with an angle of 9 degrees with a drain holes effect at 200%. In both plots the X axis represents the beam axis (Z), where the zero is the center of the drain hole.

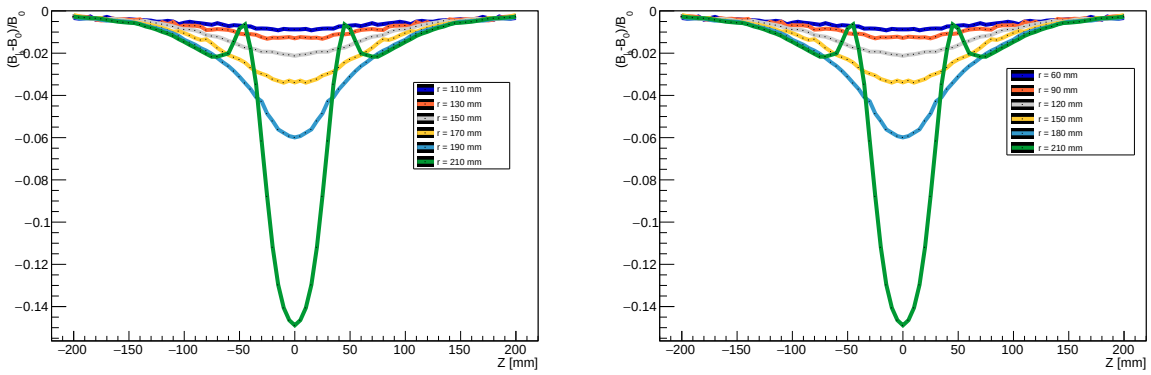

Figure A.11. Left: relative magnetic field for B_ϕ with an angle of 9 degrees with drain holes, goes for radius equal to 110 to 210 mm. Right: relative magnetic field for B_ϕ with an angle of 9 degrees with a deeper drain holes effect, goes for radius equal to 60 to 210 mm. In both plots the X axis represents the beam axis (Z), where the zero is the center of the drain hole.

Bibliography

[1] Accelerator Division Mechanical Support Dept. ANU 700KW HORN 1 NOZZLE SPRAY PETTERN 30 PSI, 2010. URL https://admscad.fnal.gov/MSDMain/DWGS/NUMI_437/pdf/437891-A1.pdf.

[2] ANSYS. Maxwell. URL https://www.ansys.com/products/electronics/ansys-maxwell.

[3] Arachne. The minerva web event display. URL http://minerva05.fnal.gov/Arachne/arachnelaunchpage.html.

[4] C. Rubbia. THE LIQUID-ARGON TIME PROJECTION CHAMBER: A NEW CONCEPT FOR NEUTRINO DETECTORS, 1977. URL http://cdsweb.cern.ch/record/117852/files/CERN-EP-INT-77-8.pdf.

[5] R. Davis. Nobel Lecture: A HALF-CENTURY WITH SOLAR NEUTRINOS, 2002. URL https://www.nobelprize.org/uploads/2018/06/davis-lecture.pdf.

[6] P. Adamson et al. The NuMI neutrino beam. *Nuclear Instruments and Methods in Physics Research Section A: Accelerators, Spectrometers, Detectors and Associated Equipment*, 806:279 – 306, 2016. ISSN 0168-9002. doi: https://doi.org/10.1016/j.nima.2015.08.063. URL http://www.sciencedirect.com/science/article/pii/S016890021501027X.

[7] F. Vannucci. The NOMAD Experiment at CERN, 2014. URL http://dx.doi.org/10.1155/2014/129694.

[8] Julián Félix. Laboratorio de Partćulas Elementales de la Universidad de Guanajuato, 2012. URL http://laboratoriodeparticulaselementales.blogspot.com/.

[9] FERMILAB. Direct Observation of NU Tau, Searching for the Tau Neutrino, . URL https://www-donut.fnal.gov/.

[10] FERMILAB. LBNF, . URL https://lbnf.fnal.gov/.

[11] FERMILAB. MINERvA, . URL https://minerva.fnal.gov/how-it-works/. Access: February 22, 2019.

[12] FERMILAB. MINOS, . URL https://www-numi.fnal.gov/.

[13] FERMILAB. NOvA, . URL https://novaexperiment.fnal.gov/.

[14] FERMILAB. NuMI facility, . URL https://web.fnal.gov/project/TargetSystems/NuMI/_layouts/15/start.aspx#/SitePages/Home.aspx. Access: February 21, 2019.

[15] O. Hann. Nobel Lecture: From the natural transmutations or uranium to its artificial fission, 1946. URL https://www.nobelprize.org/uploads/2018/06/hahn-lecture.pdf. Access: February 6, 2019.

[16] Harvard Natural Sciences Lecture Demostrations. OHP Magnetic Lines of Force. URL https://sciencedemonstrations.fas.harvard.edu/presentations/ohp-magnetic-lines-force.

[17] T. Kajita. Nobel Lecture: Discovery Of Atmospheric Neutrino Oscillations, 2015. URL https://www.nobelprize.org/uploads/2018/06/kajita-lecture.pdf.

[18] Paul Lebrun. On Focusing Uncertainties of the NuMI beam, 2017. URL https://minerva-docdb.fnal.gov/cgi-bin/private/RetrieveFile?docid=16397&filename=t1.pdf&version=1.

[19] L. Lederman. Nobel Lecture: OBSERVATIONS IN PARTICLE PHYSICS FROM TWO NEUTRINOS TO THE STANDARD MODEL, 1988. URL https://www.nobelprize.org/uploads/2018/06/lederman-lecture.pdf.

[20] A. McDonald. Nobel Lecture: The Sudbury Neutrino Observatory: Observation of Flavor Change for Solar Neutrinos, 2015. URL https://www.nobelprize.org/uploads/2018/06/mcdonald-lecture.pdf.

[21] The MINERVA COLLABORATION. Design, calibration, and performance of the minerva detector. *Nuclear Instruments and Methods in Physics Research Section A: Accelerators, Spectrometers, Detectors and Associated Equipment*, 743:130 – 159, 2014. ISSN 0168-9002. doi: https://doi.org/10.1016/j.nima.2013.12.053. URL http://www.sciencedirect.com/science/article/pii/S0168900214000035.

[22] W. Pauli. Pauli's letter of the 4th of December 1930, English, 2013. URL http://www.physics.princeton.edu/~mcdonald/examples/EP/pauli_neutrino_30_english.pdf.

[23] B. Pontecorvo. NEUTRINO EXPERIMENTS AND THE PROBLEM OF CONSERVATION OF LEPTONIC CHARGE, 1967. URL http://jetp.ac.ru/cgi-bin/dn/e_026_05_0984.pdf.

[24] F. Reines. Nobel Lecture: THE NEUTRINO: FROM POLTERGEIST TO PARTICLE, 1995. URL https://www.nobelprize.org/uploads/2018/06/reines-lecture.pdf.

[25] Sacha E. Kopp. Accelerator Neutrino Beams, 2006. arXiv:physics/0609129.

[26] M. Schwartz. Nobel Lecture: THE FIRST HIGH ENERGY NEUTRINO EXPERIMENT, 1988. URL https://www.nobelprize.org/uploads/2018/06/schwartz-lecture.pdf.

[27] J. Steinberger. Nobel Lecture: EXPERIMENTS WITH HIGH-ENERGY NEUTRINO BEAMS, 1988. URL https://www.nobelprize.org/uploads/2018/06/steinberger-lecture.pdf.

[28] The DUNE Collaboration. Long-Baseline Neutrino Facility (LBNF) and Deep Underground Neutrino Experiment (DUNE) Conceptual Design Report Volume 1: The LBNF and DUNE Projects, 2016. arXiv:1601.05471.

[29] The DUNE Collaboration. Long-Baseline Neutrino Facility (LBNF) and Deep Underground Neutrino Experiment (DUNE) Conceptual Design Report Volume 4: The DUNE Detectors at LBNF, 2016. arXiv:1601.02984.

[30] The DUNE Collaboration. Long-Baseline Neutrino Facility (LBNF)/DUNE Conceptual Design Report. Optimized Neutrino Beamline, 2017. URL https://docs.dunescience.org/cgi-bin/private/RetrieveFile?docid=4559&filename=CDR_Optimized_Beam_Oct02.pdf&version=12. Private DocDB.

[31] The MINERvA Collaboration. The MINERvA Technical Design Report, version 1.3, 2006. URL http://minerva-docdb.fnal.gov/cgi-bin/RetrieveFile?docid=700&filename=TDR_v1.3.pdf&version=28.

[32] THE MINERVA COLLABORATION. Flux Fits for NuMI Medium Energy, 2018. URL https://minerva-docdb.fnal.gov/cgi-bin/private/RetrieveFile?docid=18780&filename=Beam_Flux_Fits_ver4.pdf&version=1. MINERvA DocDB.

[33] S. Tremaine. JOHN NORRIS BAHCALL 1934 - 2005, 2011. URL http://www.nasonline.org/publications/biographical-memoirs/memoir-pdfs/bahcall-john-n.pdf.

[34] S. van der Meer. CERN Report CERN-61-07, 1961. URL https://cds.cern.ch/record/278088/files/p1.pdf. Access: February 21, 2019.

[35] Katsuya Yonehara. Measure Horn-1 field near current equalization section, 2018. BIWG meeting.

[36] Zhijing Tang. The Magnetic Field of Horn near Drain Hole, 2018.